Advances in porous perovskites: synthesis and electrocatalytic performance in fuel cells and metal-air batteries

Jie Yu, [†, #] Ran Ran, [‡, #] Yijun Zhong, [§] Wei Zhou, [‡] Meng Ni, [*, †, //] Zongping Shao [*,‡,§]

[†]Department of Building and Real Estate, The Hong Kong Polytechnic University, Hung Hom, Kowloon, Hong Kong 999077, China

[‡]State Key Laboratory of Materials-Oriented Chemical Engineering, College of Chemical Engineering, Nanjing Tech University, No. 5, Xin Mofan Road, Nanjing 210009, PR China

[§]Department of Chemical Engineering, Curtin University, Perth, Western Australia 6845, Australia

[//]Environmental Energy Research Group, Research Institute for Sustainable Urban Development (RISUD), The Hong Kong Polytechnic University, Hung Hom, Kowloon, Hong Kong 999077, China

# These authors contributed equally to this work.

Abstract: With an increasing energy demand and anabatic environmental crisis arising from the fast growth in human population and society economics, numerous efforts have been devoted to explore and design multi-functional materials for meeting high-efficiency energy transfer processes, which happen in various developed energy conversion and storage systems. As a special kind of multi-metal oxides, perovskite with attractive physical and chemical properties, is becoming a rapidly rising star on the horizon of high-performance catalytic materials with substantial research activities worldwide. The porous nanostructure in targeted catalysts is favorable to the catalytic activity and thus improves the overall efficiency of these energy-related devices. In this review paper, recent advances made in the porous perovskite nanostructures for catalyzing several anodic or cathodic reactions in fuel cells and metal-air batteries are comprehensively summarized. Plenty of general preparation methods employed to attain porous perovskite-type oxides are provided, followed by a further discussion about the influence of various strategies on structures and catalytic properties of the porous perovskites. Furthermore, we also provide deep insights gathered in the future development of porous perovskite-based materials for energy conversion and storage technologies.

1. Introduction

Along with the quick industrialization of our society and fast growth in the human population, energy demand is expanded substantially during the past decades. Up to now, our society still heavily relies on fossil fuels as the main sources of fuels, which are unfortunately non-renewable in nature, thus making them no sustainable. Furthermore, the excessive utilization of fossil fuels further brings about serious environmental concerns, such as greenhouse effect and air pollutions. From the sustainable development concern, a new green energy system is urgently needed. [1-4] Hydrogen, as a zero-emission fuel, is an ideal fuel for the future. Its combination with fuel cell technology may provide an ideal energy system for the future. [4, 5] On the other hand, electrochemical energy storage in combination with renewable energy sources like wind and solar power can provide another sustainable energy system for

our society. [6, 7] Consequently, electrochemical energy conversion and storage systems, such as fuel cells and metal-air batteries, have attracted considerable attention during the past decade. [8-10]

Fuel cells are the electrochemical energy conversion system that converts chemical energy stored in chemical bonds of various fuels into electric power in an electrochemical way without the restriction by the Carnot cycle. [11] Thus, the efficiency can be doubled as compared to conventional combustion engines. In addition, the effluent gas is much cleaner from the fuel cell device than the combustion engine. If hydrogen is used as the fuel, only water is the byproduct from fuel cells. During the past decades, various fuel cell systems have been investigated thoroughly, including the proton exchange membrane fuel cells (PEMFCs), solid oxide fuel cells (SOFCs), direct methanol fuel cells (DMFCs), and phosphoric acid fuel cells (PAFCs), and so on. [12-16] At the same time, the metal-air batteries, especially the zinc-air and lithium-air batteries were investigated extensively most recently, which can be treated as a special class of fuel cells that employ metal as the fuels for power generation. [17-19] The metal-air batteries show much higher gravimetric energy storage ability comparing to other chemical batteries, thus finding great application potential in electric vehicles. [20]

Both fuel cells and metal-air batteries contain an air electrode which plays the role of a positive electrode toward the reduction of oxygen molecules to oxygen ion (oxygen reduction reaction, denoted as ORR) in fuel cells or metal-air batteries in the discharge mode. In the charge mode in the metal-air batteries, the air electrode also functions as an electrochemical catalyst for promoting the oxygen evolution reaction (OER). The oxygen activation is a difficult process that requires high activation energy. Large polarization over the air electrode could be experienced in fuel cells or metal-air batteries, and the catalytic activity of the air electrode for ORR and OER strongly determines the cells/batteries performance. [21-23] Therefore, electrocatalysts are required to promote such reactions. Generally, precious metals are used as the active electrocatalysts in ORR, [24-27] which occurs in the cathodic part of fuel cells or metal-air batteries. Nevertheless, considering the high cost and sensitivity to CO poisoning of the precious metals, these electrocatalysts with a low cost and high performance, such as the metal oxide catalysts, carbon-related catalysts, and other non-noble metal catalysts, etc., have been extensively exploited to make the fuel cells or batteries technique more accessible to practical applications. [28-33] Among them, transition metal oxides are highly attractive and promising owing to their high stability, versatile composition, and cheap price. Considering the poor tunning capability of single metal oxides, more recently, some complex metal oxides likely perovskites have attracted considerable attention because of their flexibility in composition. [33-35]

As a particular category of complex oxides with a defined structure, perovskite-type oxides have received a great sense of attention as functional catalytic materials for numerous applications. [36-41] A typical perovskite oxide has the general formula of ABO_3, in which A site is a lanthanum element or alkaline-earth element that is in 12 coordination with oxygen ions, B site belongs to a transition-metal element in 6 coordination with oxygen. [42] The enthusiasm in perovskite oxides is that they show highly flexible elemental composition, with a large variation of properties that can be tailored by doping design. Actually, over 90% of elements

in Periodic Table of Elements can be doped into the perovskite structure. [39] For example, based on Zhu et al., little Pd-doped $LaFeO_3$ ($LaFe_{0.95}Pd_{0.05}O_3$) was successfully fabricated to offer obviously enhanced ORR activity and stability in comparison with the parent oxide-$LaFeO_3$. [43] By such doping, unusual oxidation states of 3/4+ for Pd could be well stabilized, which thus contributed to the boosted performance. Xu and his co-workers designed a series of $BaCo_{0.9-x}Fe_xSn_{0.1}O_{3-\delta}$ with the diverse Co and Fe doping concentrations as high-performance OER electrocatalysts. [44] Shao-Horn's group at MIT demonstrated the ORR/OER performance of perovskite-type oxides firmly correlates to e_g orbital occupancy, which could be regarded as a good ORR/OER performance descriptor in the design of perovskite electrocatalysts. [45, 46] It is largely dependent on the oxidation state of the B-site cation and the spin state of the electrons. Thus, they proposed that it was possible to efficiently search perovskite-type oxides which could have high activities and be viable alternative catalysts to replace precious metals in the fuel cell or metal-air power systems.

The early reports about perovskites for ORR/OER can be back several decades ago. [47-49] In 1970, Meadowcroft et al. reported La-based perovskites as the low-cost oxygen electrode material in the alkaline solution, and suggested this kind of catalysts deserved further detailed investigation both on electrode manufacture and electrical properties. [47] Although much superior area-specific activity to that of precious metal catalysts has been found for some perovskite electrocatalysts, they usually show much inferior mass-specific activity. [50, 51] This is due to the fact that the as-prepared perovskite oxides usually have very low surface area (typically lower than 5 $m^2 g^{-1}$), leading to the poor mass-transfer kinetics for ORR/OER. [52, 53] Such low specific surface area is bound up with the ionic nature of some chemical bonds in perovskite lattice and high sintering temperature is needed for the phase generation. It suggests that in order to further increase the mass-specific activity of perovskite oxides for ORR/OER, enlarging the specific surface area through advanced synthesis is required. The reduction in particle size is the easiest way to improve the surface area. However, once the particle size is dropped to the nanometer range, the current collection becomes a big challenge. Microporous/mesoporous oxides with the rich porous architecture show these advantages of high specific surface area to nanoparticles and easy current collection to that of conventional micrometer-sized particles. The rich pores could further minimize the diffusion polarization, as well as provide free pathways for oxygen transfer and electrolyte diffusion within the electrode when the oxide is used as an electrocatalyst for fuel cells or metal-air batteries. [54-56] Thus, the synthesis of porous perovskite oxides has received increasing attention during the past decade, in particular to be used as electrocatalysts for ORR/OER. [57-62]

Up to now, many attempts have been made towards the synthesis of porous perovskite oxides for functional applications, such as fuel cells, electrochemical sensors, water splitting, and metal-air batteries, etc.. [63-67] Several synthesis strategies, such as solid-state, [68] sol-gel, [69, 70] combustion, [71] hydrothermal, [72, 73] electrospinning routes, [74, 75] *et al.*, with or without surfactants and/or templates, were developed to synthesize various porous perovskite oxides. However, all the trials are dispersed and independent, which thus lack a comprehensive summary. In this article, we give an in-time overview of the recent progress in the synthesis of porous perovskite oxides, in particular towards the applications as electrocatalysts for

ORR/OER in fuel cells or metal-air batteries. Lastly, the remaining challenges and research prospects in this field are further outlined. Such review will provide useful guidance for the researchers in pursuing new synthesis techniques for porous perovskite oxides for functional applications. It may also be generalized to the preparation for other forms of metal oxides with porous structure, such as spinel and K_2NiF_4-structure oxides.

2 Synthesis of porous perovskites

2.1. Solid-state synthesis

Conventionally, perovskite oxides are synthesized through a solid-state reaction route, which is characterized by the simple process, high calcination temperature, mass production capability, and low manufacturing cost, etc. [76] For a typical synthesis, the raw materials in the solid state are thoroughly mixed and then calcine at a high temperature for sufficient time to obtain the targeted phase of perovskite oxide. In view of the significance to overcome the diffusion barrier for perovskite phase formation during the synthesis, calcination temperature of typically over 900 ^oC is required for the preparation of phase-pure perovskite oxides. [76-78] Especially, for perovskite oxides with multiple components and alkaline earth elements contained, higher calcination temperature and a prolonged calcination period of several hours is needed to gain a high-purity perovskite phase. [79-81] Such severe synthesis conditions, however, often results in poor sintering of the products with an almost pore-free structure.

To successfully synthesize porous perovskite oxides based on the solid-state reaction technique, the reduction of phase formation temperature is critical, while how to achieve high purity of the perovskite phase at reduced annealing temperature is a big challenge. Recently, two modified solid-state reaction methods, i.e., high-energy ball milling (HEBM)-assisted solid-state synthesis, [52, 81-86] and molten salts-incorporated solid-state reaction, [68, 87-89] have been proposed.

The HEBM-assisted solid-state synthesis, also called as mechano-chemical synthesis, applies mechanical energy to facilitate the solid-state reaction. During the preparation process, the reactants and the products are continuously broken into smaller particles and uniformly mixed by the mechanical force. Consequently, the diffusion barrier for phase formation is effectively reduced, and the synthesis temperature can be reasonably lowered and the specific surface area of the product may be improved effectively. For example, such technique has been successfully employed in the synthesis of various perovskite oxides for use as electrode in metal-air batteries and SOFCs. [90-93] The specific surface area, pore structure and crystalline size of the product highly depend on the ball milling time, the mass ratio of the ball to solid powder, and other operation parameters. [91-94] The main drawback of HEBM-assisted solid-state synthesis relies on that the porosity is still very low. The collapse of pores structure for a sample likely happens when undergoing the high-temperature calcination. Taking this challenge into consideration, Kaliaguine's group further modified the HEBM-assisted solid-state synthesis strategy to prepare porous perovskites by introducing various alkali additives during the ball milling process.[84, 95, 96] For instance, in 2007, the porous $LaCo_{1-x}Cu_xO_{3-\delta}$ (LCCu) perovskite

oxides were developed as catalysts for higher-alcohol synthesis. In this preparation route, group I elements were employed as alkali additives, which effectively suppressed the grain growth of the perovskite phases, and also played the role of a soft template. When washing out the alkali (alkali ions < 0.08wt%) with water, LCCu perovskite showed high specific surface area and abundant pores, so as to deliver the enhanced catalytic activity toward higher-alcohol synthesis from syngas. [84] Besides, it is noticeable that the specific surface areas of resulting products varied with the cationic radius of the alkali metal as used, nearly increasing in an order of Li < Na *(*≈Cs*)* < K < Rb, as shown in **Figure 1a**. Additionally, in the same group, a series of porous perovskite oxides including $LaFe_{0.8}Cu_{0.2}O_3$ and $LaCo_{1-x}Fe_xO_3$, etc. were also well synthesized in the presence of various additives during the ball milling processes, demonstrating the high specific surface area of about 4-105 $m^2 g^{-1}$ and improved porosity. [95, 96] Consequently, all of them displayed excellent catalytic properties for different reactions. To our knowledge, there is still no any report about adapting this attractive strategy to the synthesis of perovskite electrocatalysts in ORR or OER processes, thus requiring much attention in the future research of this field. Nevertheless, it should be noted that the impurity from the alkali additive could be potentially introduced into the perovskite phase if this novel method was applied to the synthesis of porous perovskites as electrocatalysts for ORR/OER, since most elements can be doped into the perovskite lattice, and the potential change in activity could root in such impurity doping.

In the above-mentioned reformative HEBM-assisted synthesis method with the addition of alkali, just a small amount of alkali is introduced, and thus the insufficient porosity is still produced. As the other novel solid-state synthesis strategy, the molten salts synthesis method, where alkali metal salts are used in large quantity, has attracted more eyes in the past few years, because it is considered as one of the simplest, most versatile and cost-effective approaches routes to produce crystallized, chemically purified single-phase powders at low temperatures. [68, 87-89, 97-99] The molten salt additives act not only as a soft template but also as a heating medium. [98-100] During the synthesis, salts with low melting points are mixed with the reactants in a non-solvent in the form of freshly ground crystals and then the mixture precursors are heated to above the melting point for the salt. Owing to the fact that reactants possess certain solubility in liquated salts, the molten-salt synthesis, through convection and diffusion methods, allows faster mass-transfer transport in the liquid phase, and enables reactants to be combined at the atomic scale, so as to dramatically lower the calcination temperature and shorten the sintering time. [68, 101, 102] After the pyrolysis, the salts in the resultant sample can be removed by further washing using de-ionized water several times to remove the salts, so as to achieve porous products. Typically, according to the previous studies, the weight ratios of alkali metal salts (eg. KOH, $ZnCl_2$, NaCl, $NaNO_3$, etc.) to solid precursors ranged from 1:1-15:1. [97-105] Some researchers have revealed that higher ratios may help the formation of mesopores. [100, 105] Accordingly, the particle size, morphology, porosity, and so on, could be effectively tuned in the presence of molten salts. Actually, molten salt synthesis has been successfully applied in the synthesis of perovskite oxides for decades, especially the ferroelectric oxides, such as $BaTiO_3$, $SrTiO_3$, and so on. [97] Moreover, single-crystalline $BaZrO_3$ particles have been achieved through the molten salt synthesis so that to realize the rational control of the shape of perovskite oxides. [106] Apart from these, other perovskite oxides are

fabricated as well via employing this method. [68, 97-99, 102-104] For example, Li and his co-workers reported the synthesis of $LaCoO_3$ perovskite on basis of a molten-salt solid-state precursor reaction approach. They mixed solid-state $La(NO_3)_3.nH_2O$ and $Co(NO_3)_3.6H_2O$ with a certain amount of KOH to conduct the precursors reaction, and after calcination for several hours, porous nanoparticles with the diameters of 15 ~ 40 nm were obtained. [104] Additionally, using the $NaNO_3$ and KNO_3-co-assisted molten salt route, different porous nanostructured $LaMnO_3$ including spheres and cubes, were well developed by simply altering the calcination time. [89] For example, after the calcination at 550 ^oC for 4 h, the $LaMnO_3$ showed porous spherical structure with an average pore size of about 34.7 nm (**Figure 1b** and **c**). With the prolonged reaction time to 6 h, single-crystal porous cubic $LaMnO_3$ particles were clearly observed in **Figure 1d** and **e**. The possible formation mechanisms of the different $LaMnO_3$ nanostructures had been proposed, as depicted in **Figure 1f**. It was found that the morphology had a profound influence on activity toward the catalytic removal of toluene. Song et. al recently have designed porous $La_{0.6}Sr_{0.4}Co_{0.2}Fe_{0.8}O_{2.9}$ via a simple molten-salt synthesis process (**Figure 1g**), in which the eutectic salts mixture of NaCl and KCl were employed at a weight ratio to the mixed oxide precursors of 2:1. [68] Scanning electron microscopy (SEM) images in **Figure 1h** presented porous nanoparticles interconnected with each other and the diameter of the macroporous cores was approximately 200 nm. The porous structure provided high interfacial area, which possibly exposed more active sites, thus benefiting OER catalytic behavior. Consequently, the porous $La_{0.6}Sr_{0.4}Co_{0.2}Fe_{0.8}O_{2.9}$ offered a low overpotential of 345 mV to reach a current density of 10 mA cm^{-2}, which was better than that of the benchmark IrO_2 precious metal-based catalyst (360 mV). As well, the molten salt routes were also applied for the preparation of Sr- and/or Mg-doped perovskite-type $LaAlO_3$ powders as the electrolyte of SOFC, and $La_{0.8}Sr_{0.2}MnO_3$ perovskite powders as cathode in SOFC. [87] However, it is to particularly mention that, by reported so far, perovskite oxides, successfully produced by molten-salts synthesis, still make up a very small fraction of the total perovskite oxides group, which may be due to the extremely high phase-forming temperature (sometimes even > 1000 ^oC) or the potential reaction of reactants and molten salts, and so on.

Although most of the modified solid-state processes don't mention the regulation of the pore size, the obvious increasing in the surface area and decreasing in the particle size have been obtained in them. Based on various modified solid-state synthesis routes, these targets including pure phase formation, controlled particle sizes, and corresponding specific area have been approached. However, it is difficult to achieve the controlled porosity and/or pore size due to uncontrollable and random pore-forming processes. More research in this field is needed to get understanding of the role in the molten salt synthesis, especially in the phase formation and pore formation, which then will greatly facilitate the design of porous perovskites for functional application, including in the field of electrocatalysis.

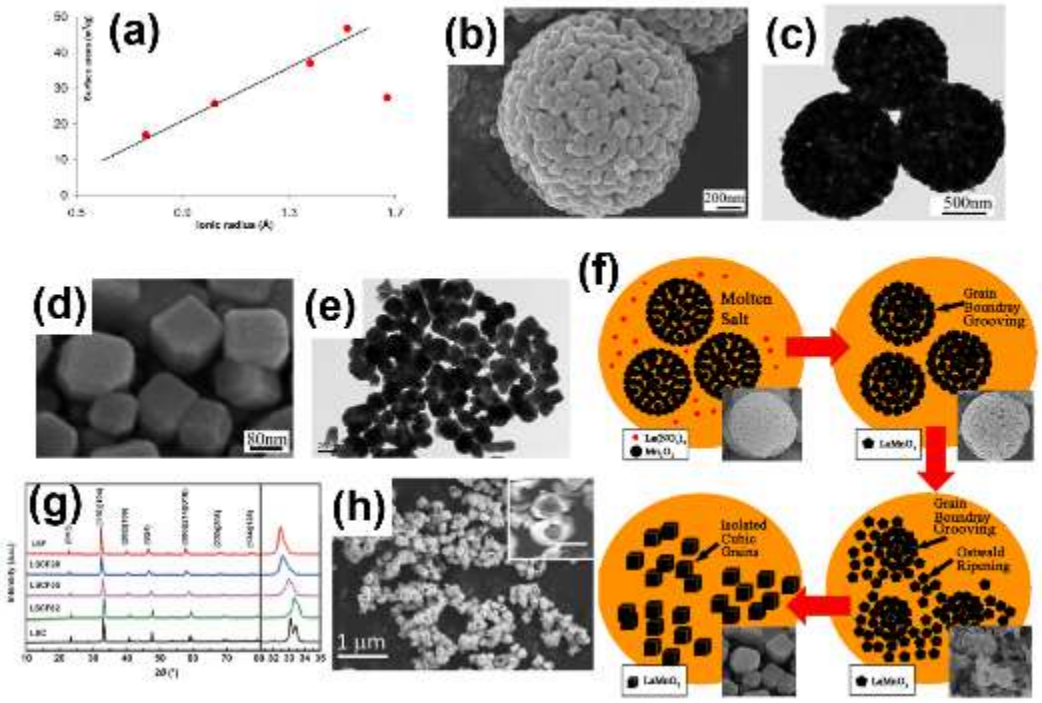

Figure 1. **(a)** The relationship between the cationic radius of the alkali metal used and surface areas of the resulting perovskite oxides. Reproduced with permission.[84] Copyright 2007, Elsevier. **(b)** Scanning electron microscopy (SEM) and **(c)** transmission electron microscopy (TEM) images of the $LaMnO_3$ sample with porous spherical structure. **(d)** SEM and **(e)** TEM images of the porous cubic $LaMnO_3$ material. **(f)** The proposed formation mechanisms of different $LaMnO_3$ nanostructures, where the $LaMnO_3$ morphology was transformed from porous nanospheres to cubic nanoparticles in molten salt media. Reproduced with permission.[89] Copyright 2014, American Chemical Society. **(g)** X-ray diffraction (XRD) patterns and **(h)** the SEM image of the as-prepared $La_{0.6}Sr_{0.4}Co_{0.2}Fe_{0.8}O_{2.9}$ perovskite with porous nanostructure. The inset in **(h)** was the corresponding enlarged image. Reproduced with permission.[68] Copyright 2018, Springer.

2.2 Wet chemical processes

The preparations of porous metal oxides through wet chemical processes have been widely exploited in recent two decades and get great progress, [56-67, 69-75] however, for multi-metal oxides, it still requires extensive investigations. Typically, most of the porous materials are produced with the presence of surfactants and templates in a solvent. After removal of the surfactants and/or templates at mild conditions and subsequent calcination steps, the solid porous materials could be successfully attained.

2.2.1 **General introduction**

Liquid solution and/or liquid precursors are always selected in the wet chemical process to form homogeneous mixtures of the raw materials. As compared to the aforesaid traditional solid-state approach, it is much easier to improve the homogeneity of the precursor mixtures at the atomic level and shorten ions diffusion path lengths during reactions, thus appropriately reducing the phase formation temperature through the wet synthesis processes and preventing the phase separation problem. [107] Among the tremendous wet chemical synthetic routes, sol-gel process, complexation method, solution combustion method, hydrothermal route,

electrospinning synthesis, and others have found particular interests in perovskite oxides synthesis to obtain the nanoparticles or controlled morphology with porous structure. [68-75, 108]

Sol-gel synthesis is one of the most powerful and widely used routes for metal oxides production, which begins with molecular precursors and then forms the targeted oxide product by the polymerization reactions. Generally, the synthesis protocols afford many merits, such as excellent nanocrystalline, good compositional homogeneity, and high phase purity. [76] In the common sol-gel route, metal alkoxides are typically employed as the precursors and are dissolved in the organic solvents. As a result, the formed uniform nanocrystals present an immense variety of sizes and shapes, like spherical, nanorods, and nanowires, etc. [108] In several previous reports, the colloidal routes to tune the morphology and grain size of metal oxides with or without surfactants have been well summarized. [108, 109] Among them, only some certain perovskite-type oxides were well developed. The review by Pinna et al. lists these materials, like $BaTiO_3$, $BaZrO_3$, $FeNbO_3$, and $SrTiO_3$, etc, [108] in which the synthesis precursors and solvents, the resulting shape, and possible reaction mechanism are also given. However, most of the as-prepared perovskite oxides are explored mainly in the fields of photocatalysis, gas sensor technology or ferroelectric materials. [110-113] Moreover, strict and complex reaction conditions are required for the sol-gel methods, which limit the wide application to design more or more complicated perovskite oxides. As another widely proposed wet chemical process, the complexion process is well established for synthesizing perovskite oxides because of the simple protocols and the universality to almost all targeted perovskite. During the synthetic procedures, complexion agents are employed to chelate with metal cations in particular solvents. [76] The citric acid (CA) is the most common used complexion agent, but other organic agents, such as poly(acrylic) acid, ethylenediaminetetracetic acid (EDTA), and other organic additives combining with citric acid are also adopted together. [114-116] Of note, some complexion methods can be ascribed to sol-gel synthesis, but generally the complexion route employs the metal nitrate or chloride salts as the precursors instead of the metal alkoxides or other organic metal salts, which extends the diversity of the metal precursors and decreases the difficulty of synthesis condition control. [43, 60, 70, 116-118] For example, Shao et al. proposed that the EDTA-CA co-complexing sol-gel strategy has been widely used to fabricate various perovskite materials, such as $LaNiO_3$, $La_{0.2}Sr_{0.8}FeO_{3-\delta}$, $Pr_{0.5}(Ba_{0.5}Sr_{0.5})_{0.5}Co_{0.8}Fe_{0.2}O_{3-\delta}$, $LaFe_{0.95}Pd_{0.05}O_{3-\delta}$, etc. [43, 116-118] Nevertheless, the complexion method has the shortcoming of not as accurate as common sol-gel method to control the particle size into nanoscale. Besides, even though such the route still cannot well regulate the porosity, porous nanostructures are achievable in some certain perovskites. For instance, according to Yang's group, the $Ba_{0.5}Sr_{0.5}Co_{0.8}Fe_{0.2}O_3$ perovskite with porous structure was developed via this EDTA-CA sol-gel method, which offered a specific surface area of 2.78 $m^2\ g^{-1}$, over 10-fold larger than that obtained by a traditional solid-state route, ~0.2 $m^2\ g^{-1}$. [70] Chen and his co-workers reported a citric acid assisted sol-gel approach to synthesize interconnected porous perovskite $CaMnO_3$ (**Figure 2a** and **b**), which demonstrated the high specific surface area of around 30 $m^2\ g^{-1}$. [60] In order to further improve the porosity and enhance the specific surface area, many researchers also modified the sol-gel complexion method via introducing some additives as a pore-creating agent, as described in the following part of templates application.

The combustion process represents another efficient and viable method for fabricating ceramic materials and other useful oxides materials, which has also been widely employed in the production of perovskite oxides. The precursors could be solid state, liquid, or gel. The typical combustion synthesis for perovskite oxide is the solution-combustion route, which refers particularly that the precursors exist in the aqueous solution form. In this process, the most frequently utilized fuels include urea, glycine, or hydrazides, etc. and a self-sustained reaction in the homogeneous aqueous solution of different oxidizers, also metal ion precursors, (e.g., metal nitrates) and fuels is involved. [76, 119] Due to the stable complexes formed between fuels and metal ions, the solubility of nitrate is increased and thus inhibits selective precipitation of the metal ions during water evaporation removal. With $La_{0.9}Sr_{0.1}MnO_3$ as an example, **Figure 2c** describes a combustion preparation process. [120] Meanwhile, the digital images showing the different steps of the solution-combustion synthesis are given in **Figure 2d**. It is noteworthy that this solution-combustion route not only yields nanosized oxides but also allows the uniform doping of trace amounts of rare-earth impurity ions in a single step. Thus, various porous perovskite nanoparticles have been synthesized through this solution combustion approach. Among the $LaFeO_3$ perovskites prepared by using different routes, the combustion method enables the biggest pore volume. [71] However, it is not so easy to control the reaction temperature, which is associated with fuel-to-nitrates ratio and fuel types. When the fuel combustion is processing, the impurities and low crystallization could be existent after the combustion reactions, and then the subsequent sintering is generally necessary in these cases. Ashok and his co-workers adopted a solution-combustion technique with the glycine as fuel to fabricate a series of $LaMO_3$ (M =Cr, Mn, Fe, Co, Ni) perovskites and found that all these as-obtained powders were porous, as shown in **Figure 2e-i**. [62] Of note, the combustion temperature for these $LaMO_3$ perovskites was largely affected by fuel to metal-nitrate ratio (φ). In comparison to other stoichiometric conditions (φ= 0.5, 1.5 and 2), the combustion temperature reached to a maximum value for all the synthesized samples, when φ equaled to 1. Lower combustion temperature led to lower crystallization. Interconnected porous $La_{0.9}Sr_{0.1}MnO_3$ (LSM) nanopowders were also prepared by Tarragó and his coworkers following a urea/sucrose-supported solution-combustion way, where LSM made with urea only as fuels enabled the single-phase formation, while these materials attained with sucrose or mixture (urea and sucrose) as fuels led directly to the obtaining of amorphous or mixed phases, respectively. Further sintering treatment helped the realization of pure phase. [120]

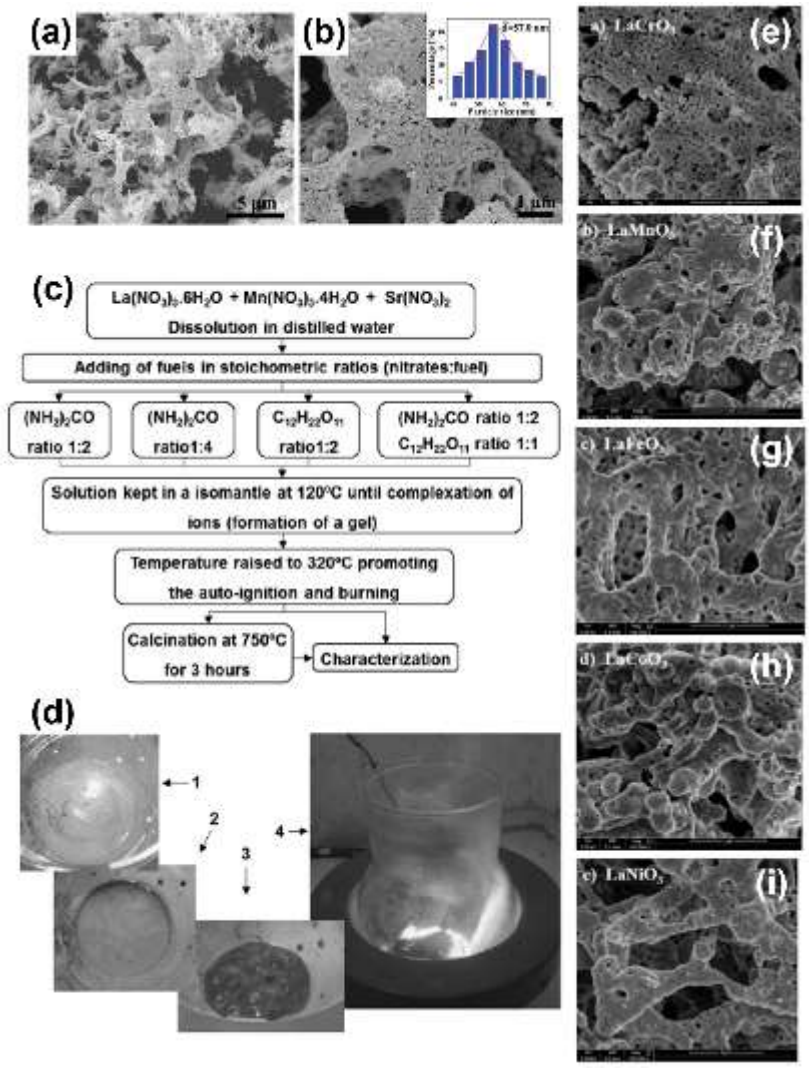

Figure 2. **(a**, **b)** SEM images of the as-obtained porous $CaMnO_3$ material. Inset in **(b)** shows the corresponding particle size distribution. Reproduced with permission.[60] Copyright 2014, Royal Society of Chemistry. **(c)** The combustion preparation process flowchart with $La_{0.9}Sr_{0.1}MnO_3$ as an example. **(d)** The digital images of the different steps during the solution-combustion synthesis: (1) water evaporation; (2) complexation reaction; (3) gel formation; (4) combustion phenomenon. Reproduced with permission.[120] Copyright 2015, Elsevier. **(e-i)** SEM images of a series of $LaMO_3$ (M =Cr, Mn, Fe, Co, Ni) perovskites. **(e)** $LaCrO_3$; **(f)** $LaMnO_3$; **(g)** $LaFeO_3$; **(h)** $LaCoO_3$; **(i)** $LaNiO_3$. Reproduced with permission.[62] Copyright 2018, Elsevier.

Other than just irregular and randomly grown particles obtained by the two approaches discussed above, hydrothermal route or electrospinning synthesis could enable a morphology-controllable preparation of perovskite oxides with the porous nanostructure. [53] Generally, a Teflon lined autoclave (**Figure 3a**) is usually used as the reactor for the hydrothermal process, in which the high-temperature (100-200 ºC) and high-pressure working conditions exist. Such pre-treatment is helpful to well crystallize perovskite oxides with a lowered annealing temperature in subsequent calcination process when comparing with the sol-gel complexation method. The electrospinning synthesis involves a specialized setup, as illustrated in **Figure 3b**, that consists of a syringe with a metal capillary tip, an electroconductive collector, and a high-voltage power supply. [63, 121] In the typical electrospinning approach, the synthesis of precursor

solution, as the first step, is crucial for the subsequent electrospinning of nanofibers, where soluble metal-salts, such as acetates, acetylacetonates, and nitrates, etc., are uniformly dispersed into an organic mixed solution with the aid of stirring, to form a transparent precursor solution. [122] Then, using the electrospinning setup at a proper humidity and temperature, the perovskite nanofiber precursor could be successfully obtained, followed by the collection and dry. Lastly, these nanofiber precursors undergo high-temperature calcination for the formation of perovskite oxides. Hydrothermal synthesis is capable of fabricating perovskite-type oxides with various miro-morphologies, like nanorods, nanospheres, nanocubes, etc. [58, 72, 123] And electrospinning helps in processing perovskites with 1D nanostructures, such as nanorods, nanotubes, and nanofibers. [63, 74, 75, 124, 125] Such tunable morphologies and the structural properties of the as-obtained perovskite oxides have a large dependence on numerous detailed synthesis conditions. In Yang's group, $LaCoO_3$ perovskites with porous particles and hollow nanospheres (**Figure 3c** and **d**) were observed via employing a hydrothermal strategy, followed by different annealing treatment procedures, as depicted in **Figure 3e**. [72] In the hydrothermal procedure, the aqueous solution with certain metal precursors (lanthanum nitrates and cobalt nitrates), were firstly mixed with glycine, and polyvinylpyrrolidone (PVP), then which was transferred into an autoclave with the Teflon liner for a heating processing at the temperature of 180 °C for 12 h. It's worth noting that glycine played the dual roles of a chelating agent and a pore-making material. Additionally, the shape, size, as well as uniformity of the resultant $LaCoO_3$ perovskite were subtly affected by the amount of used PVP and ammonia, as well as the heating treatment process. Zhen et al., adjusted the concentrations of nitrates and polyvinylpyrrolidone/polyacrylonitrile (PVP/PAN) weight ratios in the precursor solution used for electrospinning, to control the morphology of the as-prepared porous $La_{0.6}Sr_{0.4}Co_{1-x}Fe_xO_{3-\delta}$ nanofibers. [75] With the decrease of nitrate concentration, an obvious reduction in the mean diameter of the electrospun fibers could be observed in **Figure 4a**. PVP/PAN weight ratios could significantly affect the viscosity of the precursor solution. More PAN led to the more viscous solution (**Figure 4b**). Too low or too high viscosity of the precursor solution were not favorable to form clear and uniform nanofiber structures, as observed in **Figure 4c-g**. These representative examples showcase great promise for the hydrothermal and electrospinning methods in generating nanostructured perovskites with tunable morphologies and abundant porous structure. More significantly, developing some nanohybrids of perovskite oxides and multifunctional carbon are easily viable through both of the two methods, such as porous $LaNiO_3$/graphene composite based on the hydrothermal method, porous nanorod-structured $La_{0.5}Sr_{0.5}Co_{0.8}Fe_{0.2}O_3$/nitrogen (N)-doped graphene composite, and $LaTi_{0.65}Fe_{0.35}O_{3-\delta}$/N-incorporated carbon hybrid, prepared by the electrospinning route, etc. [126-128]

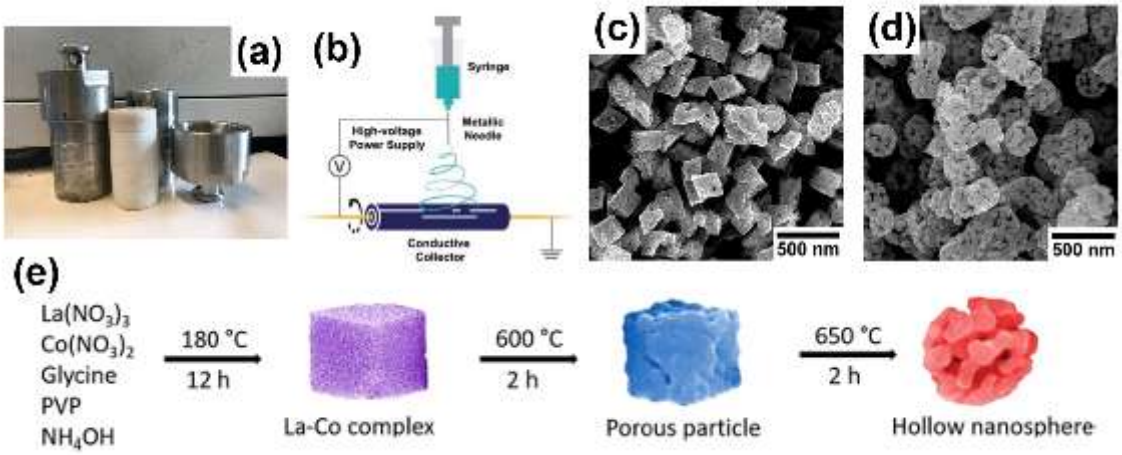

Figure 3. **(a)** A digital image showing a Teflon lined autoclave used in the experiment. **(b)** Schematic illustration of a specialized setup toward electrospinning. Reproduced with permission.[63] Copyright 2017, Wiley-VCH. **(c, d)** Typical SEM images of $LaCoO_3$ porous nanoparticles and $LaCoO_3$ hollow nanospheres. **(e)**. A schematic of the synthetic procedure for $LaCoO_3$ samples with porous particles and hollow nanospheres. Reproduced with permission.[72] Copyright 2017, American Chemical Society.

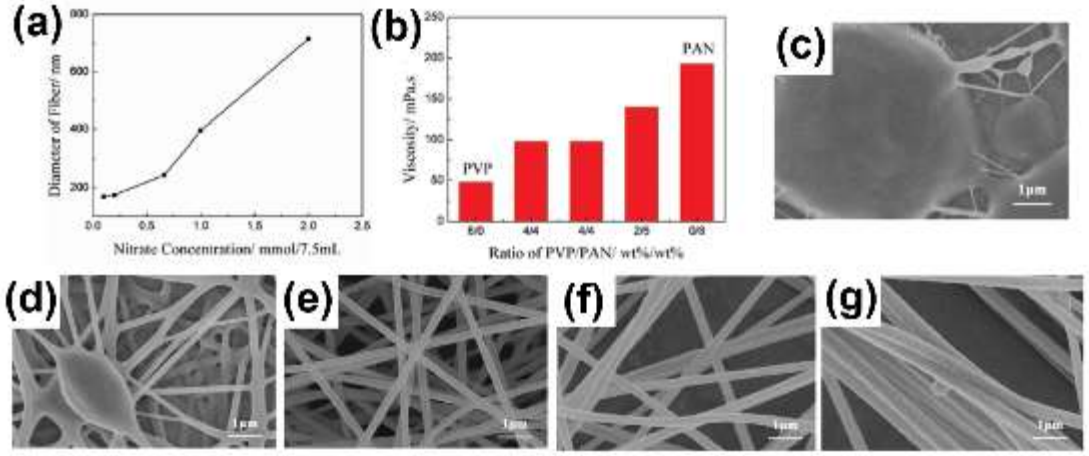

Figure 4. **(a)** The relationship between the nitrate concentration and mean fiber diameter. **(b)** The histogram exhibiting the dependence of the viscosity of the precursor solution on the PVP/PAN weight ratios. **(c-g)** SEM images of the electrospun $La_{0.6}Sr_{0.4}Co_{1-x}Fe_xO_{3-\delta}$ nanofibers before annealing with different the PVP/PAN weight ratios: **(c)** 8:0, **(d)** 6:2, **(e)** 4:4, **(f)** 2:6, and **(g)** 0:8. Reproduced with permission.[75] Copyright 2017, Wiley-VCH.

Porous substrates are also introduced to improve the porosity and surface area of the as-prepared perovskite oxides. Typically, perovskite oxides are deposited on the porous substrates such as zeolites or other oxides through the infiltration (also named as impregnation) strategy.[129-132] The supported and well-dispersed perovskites display relative higher catalytic performances in comparison with the bulk counterpart. However, in this case, the selection of the substrates should be very careful since besides the pore volume and specific surface areas, the chemical and/or physical properties of the substrates can influence the subsequent formation of ideal perovskite phases on the backstop and applied catalytic reaction process.

For example, Alifanti et al. studied the total toluene oxidation with $LaCoO_3$ perovskite nanoparticles attached on $Ce_{1-x}Zr_xO_2$ supports as catalysts, and found that the support composition had a dramatical impact on the catalytic abilities of $LaCoO_3$. [131] Actually, in most of the situations, the substrates or supports participate in the reactions by improving the oxygen mobility and/or interacting with the catalysts. [133, 134] Keav et. al have summarized these substrates, that can be reactive with the perovskite oxides or the precursors at high temperatures. [135] Of note, in SOFC, to obtain high-performance and nanostructured perovskite electrodes, infiltrating perovskite-based electrode materials into porous electrode backbone is more usually adopted. Kim et al. reported the $La_{0.75}Sr_{0.25}Cr_{0.5}Mn_{0.5}O_{3-\delta}$ (LSCM) infiltrated porous yttria-stabilized zirconia (YSZ) as a composite anode in SOFC. [132] Even though such above-mentioned perovskites are ultrafine and well-dispersed nanoparticles supported on some substrates, they don't endow porous nature. Several particular cases are given to illustrating the synthesis of porous perovskite by infiltration. [136, 137] Lu et al. adopted the infiltration way to fabricate porous spherical $La_{0.8}Sr_{0.2}MnO_3$ by using porous MnO_2 sphere as supports. [136] The porous MnO_2 was prepared by a similar molten salts-incorporated solid-state reaction. **Figure 5a** illustrates the total growing process of porous spherical $La_{0.8}Sr_{0.2}MnO_3$. Besides, mesoporous $La_{0.8}Sr_{0.2}MnO_3$ nanosheets hybridized with graphene to form sandwich-like nanosheets (G/meso-LaSrMnO) was reported by Yang and his co-worker. In its preparation (**Figure 5b**), a dip-coating method was also involved. [137] First, the support of porous graphene foam (G-foam) was obtained via using a modified Hummers way and a subsequent hydrothermal treatment. Then G-foam was immersed into a mixed precursor solution containing various metal nitrates and surfactant F127. With the solvent evaporation, metal precursors were coassembled around the arranged surfactant micelles and generated a continuous mesophase. At the same time, the added concentrated HNO_3 and citric acid, as the coordination agent, well dominated slow hydrolysis and condensation of the precursors, so as to help the heterogeneous nucleation of $La_{0.8}Sr_{0.2}MnO_3$ on graphene sheets. After segmented calcination at the different temperatures, a hierarchical 3D porous G/meso-LaSrMnO structure was attained, as shown in **Figure 5c-e**.

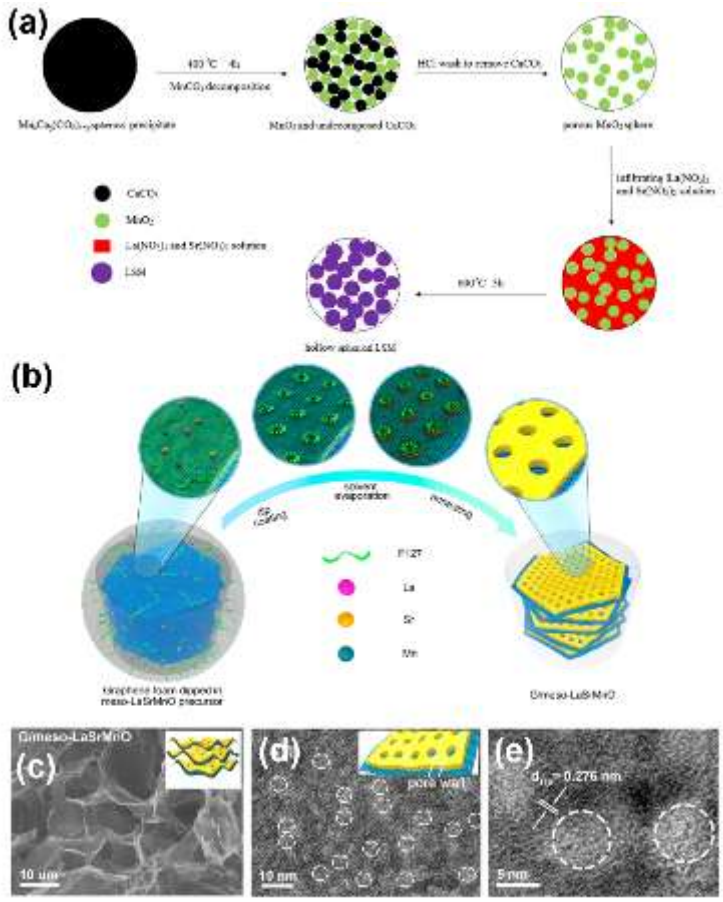

Figure 5. **(a)** The diagrammatic drawing for the construction of porous spherical $La_{0.8}Sr_{0.2}MnO_3$. Reproduced with permission.[136] Copyright 2014, Elsevier. **(b)** Schematic diagram showing the growing routes of the G/meso-LaSrMnO sample. **(c)** SEM image and **(d, e)** TEM image at low **(d)** and high **(e)** magnifications of the hierarchical 3D porous G/meso-LaSrMnO catalyst. Reproduced with permission.[137] Copyright 2015, American Chemical Society.

Since the synthesis routes have an impressive effect on the properties of as-obtained products, different modified methods are selected for diverse targets, such as to improve the purity of phase, enhance the semi-conductivity, increase the surface area, decrease the grain size, promote the electrocatalytic reaction, and so on. For example, in order to improve the homogeneity of substitution of strontium, Baythoun *et.al.* developed stronitium-substituted lanthanum manganite perovskite oxides through the amorphous citrate processes. [138] It was demonstrated that its homogeneity was better than that from the freeze-drying or conventional thermal decomposition processes. Besides, with the increase of the heating temperatures to remove carbon, a significant reduction in surface area was occurred, which is not desired if the perovskite oxides will be applied in a catalytic procedure. Zhou et al. reported the size-controlled $LaCoO_3$ perovskites constructed by tuning the annealing temperatures as the OER electrocatalysts. [139] For the ferroelectric oxides, the phase purity and the crystalline size are critically required during the application. Hydrothermal routes are attempted to produce the ideal materials with controllable morphology and particle size. [53, 140] Mao et al employed the hydrothermal synthesis to develop perovskite nanotubes. [141] TiO_2 nanotube was applied as a bona fide precursor to form $BaTiO_3$ and $SrTiO_3$ nanotubes, and the outer diameter and inner

diameter ranges of the nanotubes was 8-15 nm and 4-7 nm, respectively. Nevertheless, small amounts of impurities were detected, which meant that further modification of the synthesis parameters was still required.

In the past decades, much effort has been devoted to study porous perovskite oxides as heterogeneous catalysts. Porous nanostructures with numerous unique characteristics can greatly favor the inherent performance of solid materials. Thus, as compared to the corresponding bulk counterpart, they exhibit more attractive catalytic activity in many important catalytic reactions, such as NO_x reduction reactions, CO and light hydrocarbons oxidation, water-gas shift reactions, OER, ORR, and hydrogen evolution reaction (HER) etc. [58, 63, 72, 75, 142-144] For their applications in the electrocatalysis field, properties such as well crystallinity, high phase purity, bi-function for catalysis, good conductivity, and robust stability in the harsh electrolyte environment, are highly desired. Consequently, the corresponding synthesis routes, which can conduct these targets, are pursued. The detailed progress about the porous perovskites in electrocatalysis of the fuel cell and metal-air battery could be seen from the **Forth Section**. As well-known, abundant porous channels can promote the mass/fluid/gas transfer and/or provide more catalytic active sites, and thus enhance the electrocatalytic performance. To further realize the high porosity and ordered pore structures in solid oxide catalysts, templates are very welcome in the preparation procedure.

2.2.2 The templates application in the synthesis of porous perovskites

Since the beginning of the last century when the ordered porous molecular zeolites were first successfully synthesized, this novel technology holds great promise for the fabrication of various materials with mesoporous structures, even for porous multi-metal oxides. Generally, the templates applied in the synthesis of porous perovskites can be catalogued as two types: soft template and hard template.[145-155] The organic surfactants or their supramolecular assemblies, such as PVP, Pluronic P123 triblock copolymer, cetrimonium bromide (CTAB), etc., employed for the formation of the porous materials are denoted as 'soft template'. [145-148] In 2011, Pal et al. successfully developed the mesoporous $ZnTiO_3$ perovskite through an evaporation-induced self-assembly (EISA) method, in the presence of an organic template P123. [145] After successful self-assembly, the as-obtained solid precursor would undergo slow heating and calcination at 400 ºC, and thus the nanostructure $ZnTiO_3$ was easily formed with the dimension of pores varying from 5.0 to 5.5 nm. By this similar method, Zhang and his co-workers also illustrated the preparation of porous perovskite-type $La_{0.75}Sr_{0.25}MnO_3$ nanotubes, with the adoption of PVP as soft template. [146] They demonstrated that the porosity could be further tuned by the amount of PVP. Meso-macroporous $LaMnO_3$ particles and microporous $La_{0.8}Sr_{0.2}MnO_3$ nanorods were also constructed via using soft templates of P123 and CTAB, respectively. [147, 148] **Figure 6a** describes the preparation process of microporous $La_{0.8}Sr_{0.2}MnO_3$ nanorods, in which an interfacial self-assembly process between metal cations, OH^- and CTAB were first carried out, followed by hydrothermal and annealing treatment. Normally, during the soft template-assisted synthesis, the templates are introduced to the precursor or the reactants and then are confined in the growing solid products. Besides, the homogeneous mixing of the starting sol or solution appears easier to be acquired with the aid of the chelating agents or organic templates. While the heating treatment is performed to realize the phase formation, the

templates are *in-situ* eliminated and leave a pore system. Such templates are also defined as 'endotemplate' by Schuth et al. [149]

As the pre-requisite, the phase purity is a big concern for the porous perovskites. However, organic surfactant templates usually decompose below the crystallization temperatures of the perovskite-type metal oxides. Consequently, while ensuring the high-purity phase under high-temperature calcination, the mesostructure easily collapses during the pore wall crystallization or the lack of support. Considering this potential possibility and in order to form the uniform pore structures, alternative synthesis routes are developed with the 'hard materials' as templates. During this procedure, mesoporous silicas, such as KIT-6, SBA-15, etc., polystyrene sphere (PS), polymethyl methacrylate (PMMA), carbon-based materials, and so on, are usually adopted as the 'hard template', and ordered porous structure could be easily realized when evenly arraying these hard templates. [57, 150-155] Noteworthily, relative to the use of soft templates, the 'hard template'-assisted route makes the synthesis simpler to be controlled, so as to reap the targeted products.

Nanocasting method is considered as one of the most effective pathways to gain uniform porous structures in this hard-templating technology. It generally contains several steps, for instance, synthesis of the template materials, impregnation of the precursor solution including metal ions into the template's channels, generation of ideal products, and finally hard template removal. In 2008, Wang et al first prepared ordered mesoporous $LaCoO_3$ by using the nanocasting method with a 3D mesoporous cubic (Ia3d) vinyl silica as the hard template. [150] The La-Co citrate complex precursor was filled into these mesopores in the silica template, and then they went through the calcination and template removal. As a result, the targeted perovskite $LaCoO_3$ showed a large specific surface area of ~ 97 m^2 g^{-1}, and a very narrow pore size distribution with the peak lay at around 6 nm, which was wider than the wall of the silica template (~3 nm). Later, according to Nair et al., ordered mesoporous KIT-6 silica was also used as a hard template for nano-structural engineering of a series of mixed metal perovskite oxides $LaBO_3$ (B=Mn, Co, Fe) with porous frameworks via the nanocasting strategy. [151] The high values of specific surface areas ranging from 110 to 155 m^2 g^{-1} were gained for the resulting materials. In recent years, through the direct hydrolysis of tetraethoxysilane (TEOS) to form silicas-based hard template, porous perovskite $Ba_{0.5}Sr_{0.5}Co_{0.8}Fe_{0.2}O_{3-d}$ (BSCF) was well fabricated by Yang and his co-worker, as schematically depicted in **Figure 6b**. [57] It was found that the specific surface area of the as-prepared BSCF was varied with the TEOS to BSCF precursor ratio, presenting a 'volcano'-like trend (**Figure 6c**). PMMA, as an interesting template that can create a 3D ordered macroporous (3DOM) architecture in perovskite oxides, has attracted extensive attention. [65, 67, 155] Lately, Dai and his co-workers reported the preparation of 3DOM-structured $LaFeO_3$ perovskite, where the template of monodispersed PMMA spheres with an average diameter of ≈330 nm was infiltrated with metal precursor solution, followed by drying, calcination, and template elimination, and subsequently $LaFeO_3$ perovskite with 3DOM nanostructures were successfully achieved (**Figure 7a**). [155] Shown in the **Figure 7b** and **c** is the typical scanning electron microscopy (SEM) and transmission electron microscopy (TEM) images, which revealed the apparent honeycomb-like morphology with well-ordered and interconnected pore channels. Such porous architectures endow the

material with high surface areas, which will offer more accessible active sites, and favorable reactants/electrolyte transport tunnels, etc., so as to help the electrocatalysis.

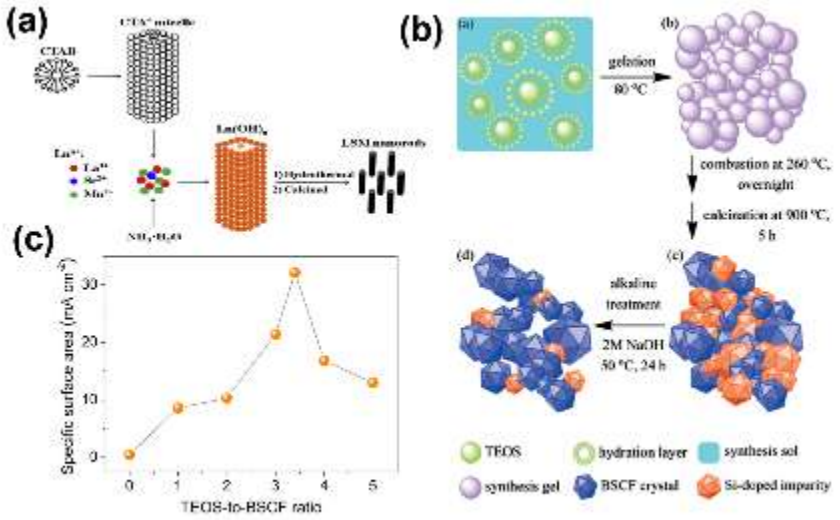

Figure 6. **(a)** Schematic description for the synthetic route of microporous $La_{0.8}Sr_{0.2}MnO_3$ nanorods. Reproduced with permission.[148] Copyright 2015, Elsevier. **(b)** Schematic diagram of the preparation of the porous $Ba_{0.5}Sr_{0.5}Co_{0.8}Fe_{0.2}O_{3-d}$. **(c)** Plot revealing a relationship between the specific surface area and the TEOS to BSCF precursor ratio. Reproduced with permission.[57] Copyright 2015, Wiley-VCH.

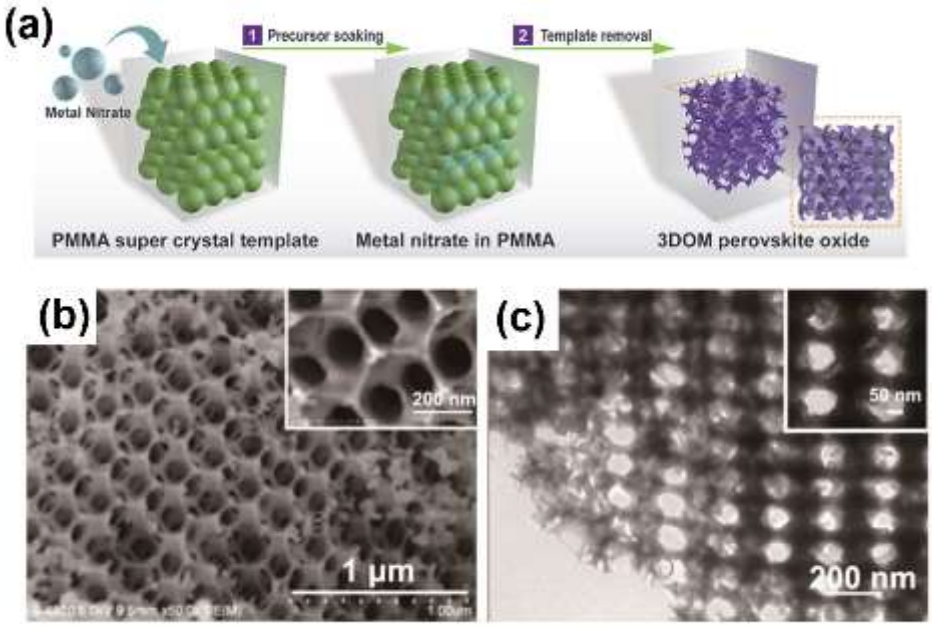

Figure 7. **(a)** A schematic of the synthesis for $LaFeO_3$ perovskite with 3DOM nanostructures. Representative **(b)** SEM and **(c)** TEM images of 3DOM-structured $LaFeO_3$. The corresponding magnified images were shown in **Insert**. Reproduced with permission.[155] Copyright 2019, Wiley-VCH.

As a summary, the template-assisted nanocasting method can fabricate ordered porous perovskite oxides, which commonly possess a large surface area due to the presence of

abundant pores, and the porous size could be well modulated based on the type of templates. Additionally, it should be highlighted that although most of the cases are not exactly the replica of the hard templates, the resulting materials still offer much more ordered porous structures and improved specific functions. However, there are still some challenges in this template-assisted preparation that are needed to be worked out. First, the selection of the template is of great significance, which should keep stable in the high-temperature environment. For sake of the acquisition of a pure perovskite phase, the selected template should not react with the perovskite precursors or oxides. For example, the introduction of Si-type templates, such as TEOS, into some perovskite precursors could allow Si-doping and thus bring about the segregation of secondary phases like $Sr_2CoSi_2O_7$. [57] Besides, the template should be facile to be removed, thereby that would not affect the purity of the targeted perovskite oxides and destroy the required pore structure. Taking these into consideration, the study of suitable templates still has a long way to go.

Given that the removal of the hard templates needs an additional treatment process, that was environmental-unfriendly and time/energy-consuming. [53] Especially, for the silica-type hard templates, the removal conditions seem extremely harsh (under strong alkaline conditions or by HF), which are very dangerous for operators. Accordingly, porous carbon provides a more facile and alternative route for the hard-templating approach to create porous materials. Carbon could be mildly eliminated through a simple combustion route or by reacting with other reactive gases. Schwickardi et al. conducted the activated carbon impregnation process with metal salt solutions. [156] After carbon removal by calcination, porous multi-metal oxides were successfully produced. Among them, the $LaFeO_3$ perovskite material has a BET surface area of ~ 49 $m^2 g^{-1}$. It was believed that narrow pores of activated carbon effectively prevented the growth of large particles in the heating-treatment process, which then contributed to the relatively high surface area. Additionally, Shao et al. proposed an *in-situ* sol-gel derived carbon templating method to fabricate highly porous perovskites nano-particles of $La_{0.6}Sr_{0.4}Co_{0.2}Fe_{0.8}O_{3-\delta}$ and $La_{0.8}Sr_{0.2}MnO_{3-\delta}$. [154] In this synthesis, these raw materials were mixed via the EDTA-CA complexing route, and then are pyrolyzed at the moderate temperature in the oxygen-deficient environment to simultaneously generate the perovskite oxide and convert the organic precursor into carbon. After further high-temperature calcination under air, the high-purity perovskite phase was achieved and the resulting carbon was burned out to create highly porous structure in the perovskite framework. Later, in the same group, a combusted cellulose-like carbon templated synthesis strategy was also reported to prepare hierarchical porous $SrNb_{0.1}Fe_{0.9}O_{3-\delta}$ perovskite electrode. [66] Even with these cases, owing to the relatively low decomposition temperature of carbon, these perovskites with a high phase-forming temperature allow no obvious porous architecture when using carbon as templates. In addition, the ordered porous structure is difficult to be observed in the carbon templated-mediated synthetic procedure.

2.2.3 The synthesis of porous perovskite oxides without templates

Apart from the synthesis strategies mentioned above, other template-free approaches are also extensively investigated. [64, 157, 158] Zou et al applied a new strategy based on the EISA (evaporation-induced self-assembly) approach to manufacture porous $SrTiO_3$ and $BaTiO_3$

perovskites. Taking the $SrTiO_3$ as an example (**Figure 8a**), excess Sr precursor was added into the raw solution in the preparation route, and with the solvent evaporation and annealing, then partially reacted to generate the $SrTiO_3$ phase and partially turned into $SrCO_3$ nano-grains dispersed in the $SrTiO_3$ sample. [157] Following the dissolution of the carbonate by using acid, mesostructured $SrTiO_3$ could be formed. Edwards's group et al has designed a mesoporous N-doped $SrTiO_3$ perovskite on basis of a template-free synthesis, and in such process, glycine was used not only as a nitrogen source but also as a mesopore creator. [158] Zhao and his co-workers fabricated $La_{0.5}Sr_{0.5}CoO_{2.91}$ perovskite nanowires with a hierarchical mesoporous structure as a high-performance ORR catalyst, via employing a simple multistep microemulsion approach with metal nitrates precursors ($La(NO_3)_3{\cdot}6H_2O$, $Sr(NO_3)_2$, and $Co(NO_3)_2{\cdot}6H_2O$) and KOH, followed by a slow calcination at 800 ^oC. [64] The unique porous architecture endowed this material with the disorder-free channels of oxygen vacancies that could enhance ORR electrocatalytic activity and the performance of Li-air batteries. In recent years, based on the Lu et al.'s study, lanthanum-transition-metal perovskites (denoted as $LaMO_3$, M=Fe, Co, Ni, and Mn) with robust meso-scale porous structures (meso-$LaMO_3$) were successfully constructed by a promoted electrostatic self-assembly with the ionic liquid as soft medias, connected with subsequent extraction and calcination at high temperatures (**Figure 8b**). [159] As exhibited in **Figure 8c-f**, well-crystallized perovskites with wormlike mesoporous frameworks were well observed. This investigation supplies a new strategy for the synthesis of porous perovskites without the application of the toxic or environment-unfriendly templates, although controllable porosity and pore collapses are still the main problems since the ionic liquids are evacuated before calcination steps.

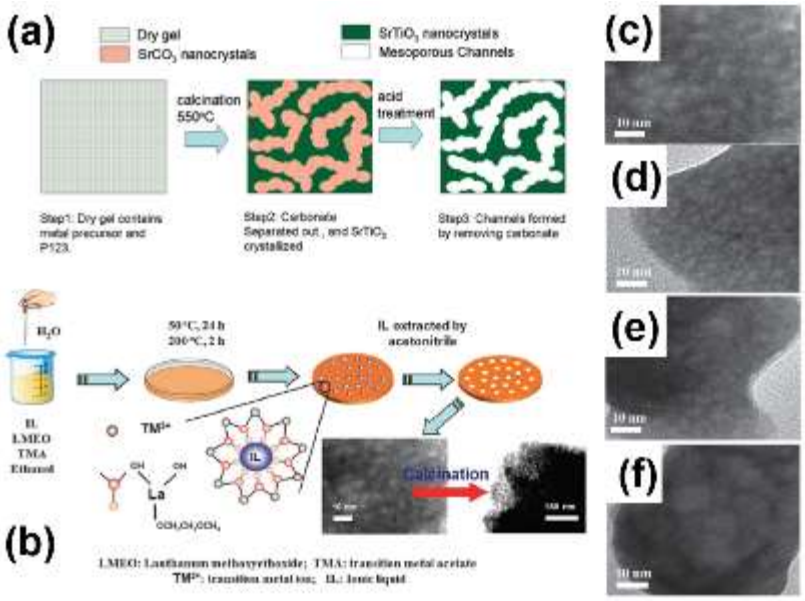

Figure 8. **(a)** Schematic illustration of the growing mechanism of porous $SrTiO_3$. Reproduced with permission.[157] Copyright 2010, American Chemical Society. **(b)** Synthetic procedure of these meso-$LaMO_3$ (M=Fe, Co, Ni, and Mn) samples **(c-f)** TEM images of the as-prepared meso-$LaMO_3$ (M=Fe, Co, Ni, and Mn). **(c)** $LaMnO_3$, **(d)** $LaFeO_3$, **(e)** $LaCoO_3$, **(f)** $LaNiO_3$. Reproduced with permission.[159] Copyright 2015, Royal Society of Chemistry.

3 The influence of pore structure and morphology on the catalytic performance

Given that the porous structure and special morphology in catalytic materials endow these materials with extensive merits of more exposed active sites, facile accessibility to the electrolyte, and favorable mass/charge transfer, etc., excellent catalytic performances for such materials in certain energy-related application are easily realized. Up to now, the investigations of controllable pore structures and tunable morphologies in various materials have been carried out for decades. In order to improve the electrochemical properties of the electrocatalysts in various rechargeable batteries and fuel cells, it is preferred to construct the structure of the electrodes or the catalysts into nanostructures with the featured morphology and favorable porosity. Numerous studies have already revealed that such nanostructure conveys a significant influence on the electrochemical behavior in the batteries. Chan et al. have grown the Si nanowire anode directly on the metallic current collector substrate, and demonstrated a higher capacity and improved stability toward rechargeable lithium batteries, in comparison with other forms of Si anodes. [160] Li et al. investigated the Ni-doped Co_3O_4 nanowires as the OER electrocatalysts, in which, it was believed that the open nanowires space can facilitate the diffusion of the active species, and the enlarged surface of the mesostructure can promote the surface reactions, so as to enhance OER performance. [161] According to Song et al., a comparison study between cube- and plate-shaped Co_3O_4 catalyst was conducted for lithium-oxygen (Li-O_2) batteries. [162] The different shape-controlled materials induced diverse surface atomic configuration and active-site charge distribution, thus dominantly affecting the properties of Li-O_2 batteries. Such results proved that the electrocatalytic activity depended strongly on the structure and morphology of the materials.

As known to all, the different synthesis routes could lead to different pore structures and surface morphologies. At the same time, different pore-makers play a crucial role in forming the pore architecture and the morphology as well. Thus, it is well understood that the as-obtained products display various micro-morphology and micro-structures, including the distribution of pores, pore size, uniform degree of the pore, grain size, surface area, and microcosmic shape, etc. As to the general controllable synthesis for nanostructure, some modified solid-state reactions such as HEBM-assisted one and molten salts-incorporated one, the sol-gel complexation process, the combustion method, the hydrothermal route, and even the electrostatic spinning, etc., with sometimes introducing pore-creating templates, are applied to construct various desired morphologies, as discussed above. Consequently, porous perovskites with nanotubes, nanowires, nanocubes or nanospheres, etc. have been successfully developed as the high-performance ORR or OER catalysts, which might show promise for applications in various rechargeable batteries and fuel cells, but it is still lack of systematic comparing work for these porous perovskite-type oxides with featured morphology to meet different purposes as electrocatalysts. On basis of the catalytic reaction processes, it is clearly found that the formation of the hierarchical pores correlated with large pore volume and high specific surface area is very necessary, in which plentiful large pores help to facilitate the continuous diffusion of the reactants and the products, and numerous small tunnels offer phase triple-boundaries for ORR or OER in fuel cells or other rechargeable batteries. Moreover, the solid products for the discharge process in metal-air batteries (for instance, basically Li_2O_2 in the Li-air battery, ZnO in the Zn-air battery) will be limited by the pore size, if the pores are too small, which will clog the pores so that to hinder the transportation of the reactants and the

products. [163] Meso-/Macro-porosity is believed as the ideal pore size to offer the compromising transfer channels, maximizing active sites, or even as substrate, to accommodate solid products (such as Li_2O_2, ZnO). [163] Park et al., employed two mesoporous carbons with different pore sizes, CMK-3 and MSU-F-C, as cathodic catalysts of Li-O_2 batteries to study their effects on these discharge products and the resultant batteries performance. [164] In such structure, discharge products were well confined within the pore channels, and the sizes of the discharge products formed at the CMK-3 electrode are smaller than those in MSU-F-C as a result of the smaller pore structures of CMK-3. Due to smaller lithium oxides, the charging potentials were lowered. When compared with that found from the small pores in CMK-3, the 3D-interconnected large pores in MSU-F-C provided faster mass transport, and thus reduced the charging potentials at a high current density and improved the rate capabilities. These results suggested that regulation of the porous architecture is very essential to boost the performance of the Li-O_2 battery. Kim et al. reported that the platinum electrode with ordered macroporous architecture in fuel cells delivered an adequate porosity, an enhanced mass transfer, as well as more effective water management, so resulting in enhanced cell performance. [165] Besides, the morphology is also of big importance for the deposition of the discharge products (such as Li_2O_2) on the surface of the catalysts, which could tightly cover the catalyst particles and thereby hamper active sites, and some of which are insulated. For example, in shape-controlled Co_3O_4 materials, the discharge product grew minimally on surface of the Co_3O_4 cube, owing to the relatively large surface energy of the edge, while the surface of the Co_3O_4 plate presented perfect encapsulation by these products with a lamellar shape, but that favored the fast electron transfer. [162] In a word, the desirable electrode structures should incorporate favorable shape and abundant hierarchical pores from microscale to macro-/meso-scale to help to overall electrocatalysis.

4 Electrocatalysis of porous perovskites in fuel cells and metal-air batteries

Perovskite oxides possess many attractive natures that endow them with excellent catalytic performance in various applications, such as photocatalysis, electrocatalysis, heterogeneous catalysis, gas sensor, and hydrogen peroxide detection. [40, 166-170] Over recent years, researchers also discovered the photovoltaic application of the perovskite oxides-based solar cells. [171, 172] And as some of the most appealing properties, the electronic and ionic conductivity, as well as the tunable composition and structure make these perovskite oxides to be the promising candidate as the electrocatalysts for ORR and/or OER in various electrochemical systems. Here, the final target of fabricating porous architecture in perovskite-type catalysts is to enhance the electrochemical performance. For sake of presenting a better overview about developing porous perovskite oxides for electrocatalysis, a plethora of examples in which the catalysts with tunable morphology and porous structure were prepared by using the above-mentioned routes for boosting ORR and/or OER reactions in fuel cells and metal-batteries were illustrated in details in the following section.

4.1. Fuel cells

Fuel cells have been identified as one of the most promising energy power devices in the future, in which chemical energy stored in chemical bonds of various fuels can be well converted into

the applied electrical energy by a fuel oxidation reaction at the anode and an ORR on the cathode. Fuel cells contain various forms of systems, such as SOFCs, PEMFCs, DMFCs, and PAFCs, etc. [173] Among them, SOFCs exhibit plenty of distinguished merits over others, like low cost, high efficiency, and fuel flexibility. Generally, in a SOFC system, hydrogen or hydrocarbons are used as the fuel, and through a chemical interreaction between anodic fuel and cathodic oxygen, water or water and CO_2 are the final products. [174] Besides, as to the catalyst materials in such system, perovskite oxides are the most extensive choice for promoting the anodic fuel oxidation and cathodic ORR. However, the bulk nature could bring about the sluggish oxidation/reduction reaction at electrodes. Thus, building these perovskite oxides with porous nanostructure is a viable strategy to realize the sharply enhanced performance.

As to the cathodic ORR field in SOFCs, at early stage, Adler et al. have discussed the ORR mechanism at a porous perovskite oxide electrode with the continuum modelling and found that for the best electrode material of $La_{0.6}(Ca, Sr)_{0.4}Fe_{0.8}Co_{0.2}O_3$, extension of the reaction zone beyond the three-phase boundary was restricted to a few micro-meters. [175] The modeling results also revealed that gas-phase diffusion resistance significantly contributed to the cell impedance at $P_0 \leq 0.1$ atm. However, the porous perovskites as the electrode materials of SOFCs were still experimentally absent in subsequent ten years. In 2000, the mesoporous multi-metal oxides with the fluorite structure of YSZ were built up firstly and used as the electrodes in SOFCs by Mamak et al. [176] They believed that the porous YSZ materials might significantly improve the fuel/oxidant mass transport, oxide ion mobility, electronic conductivity, and charge transfer during the SOFC operation process, and thus the operating temperature could be much lowered. Later, Zhang et al. also constructed the dual-scale porous electrode with the polymer foams as the templates, which was applied in intermediate-or low-temperature (IT) SOFC. [177] It was well demonstrated that the multiscale porous mixed conductors were ideally suitable for electrode applications. Macroporous structure promoted rapid gas transport through the porous electrodes, while mesoporous framework provided high surface areas for gas adsorption/desorption and more catalytically active sites for electrode reactions. Based on these pioneering studies about the porous cathodic electrodes in SOFCs, then some perovskite oxide-based porous multi-metal electrodes have been also investigated. [66, 69, 178-185] For example, Chen's group directly grew the porous nano-network of MIEC-type perovskite $Sm_{0.5}Sr_{0.5}CoO_{3-\delta}$ (SSC) on a $Sm_{0.2}Ce_{0.8}O_{1.9}$ (SDC) skeleton through infiltrating. The infiltrated SSC nano-network comprised well-connected SSC nanowires generated from nanobeads with an average size of around 46 nm, thus providing a continuous path for both O^{2-} ion and electron transportation. [178] As a result, a good triple phase boundary (TPB) was formed and a remarkably high ORR activity was gained. Following this work, the same group further used a combined route of vacuum-free infiltration and succedent freeze-drying combustion to construct a hierarchically porous cathode of SSC nano-network on a $Gd_{0.1}Ce_{0.9}O_{2-\delta}$ (GDC) backbone. [182] During the synthesis, an SSC metal ions-precursor solution was first prepared with a glycine additive as the metal ion-chelating agents and subsequent pore-makers during combustion process, and then it was infiltrated into GDC backbone, followed by freeze-drying treatment to efficiently protect the primary morphology and porous structure, and subsequent combustion to form the products. The SSC powders obtained by this approach presented very

fine particles with porous microstructure, as shown in **Figure 9a** and **b**. Benefitting from porous SSC-GDC architecture at the cathode, mass transport was promoted, effective TPB length was extended, and active sites were enlarged, thus resulting in a large ORR optimization. Consequently, in the SOFCs performance evaluation, it achieved a high peak power density of 1.44 Wcm^{-2} and a low polarization resistance of 0.05 Ω cm^2 operating at 600 °C, which was much better than that of other cells with SSC-GDC cathode made from TC (traditional-combustion without glycine), TC-G (traditional-combustion with glycine) and FC (freeze-drying combustion without glycine) routes (**Figure 9c** and **d**). Additionally, Jiang et al. also constructed a 3D hierarchical porous $SrNb_{0.1}Fe_{0.9}O_{3-\delta}$ (SNF-3D) to enhance the performance of ORR electrode in SOFCs, which was built by a combusted cellulose-like carbon templated synthesis route (**Figure 9e**). [66] SEM images elucidated the 3D microstructure with aperiodic dual-scale macropores with the diameters of 0.5-1 m and 50-200 nm. Owing to more exposed active areas and better gas transport channels from such structure, the cathodic ORR activity was well optimized with reaching a targeted area-specific resistance (ASR) value of 0.15 Ω cm^2 at 600 °C. In 2017, according to Liu's group, a porous $La_{0.6}Sr_{0.4}Co_{0.2}Fe_{0.8}O_{3+\delta}$ (LSCF) nanofibers cathode was designed for SOFCs via a controllable electrospinning technique strategy (**Figure 10a**). [183] Shown in **Figure 10b** is its TEM image, which revealed that the LSCF fibers with diameters of approximately 200 nm were made up of nanoparticles and pores both with sizes of about 50 nm, thus affording a larger specific surface area. As compared to the commercial bulk counterpart and the crushed fibers, the unique porous LSCF cathodic framework boosted the ORR activity by favorable mass/charge transport, concretely delivering a smaller ASR and a lower activation energy barrier (**Figure 10c** and **d**). Such results were further verified by geometric modeling and simulation research. Moreover, an excellent single cell performance with a peek power output of nearly 0.62 W cm^{-2} and 450-h stable operation at a fixed potential of 0.7 V at 600 °C was realizable with LSCF nanofiber as the cathode, which obviously surpassed that of the other two samples (**Figure 10e** and **f**). Very recently, Li et al. found that infiltrating a certain amount of SSC into porous layered perovskite $(PrBa)_{0.95}(Fe_{0.9}Mo_{0.1})_2O_{5-\delta}$ (PBFM) to form a composite material could largely facilitate the ORR process. [184]

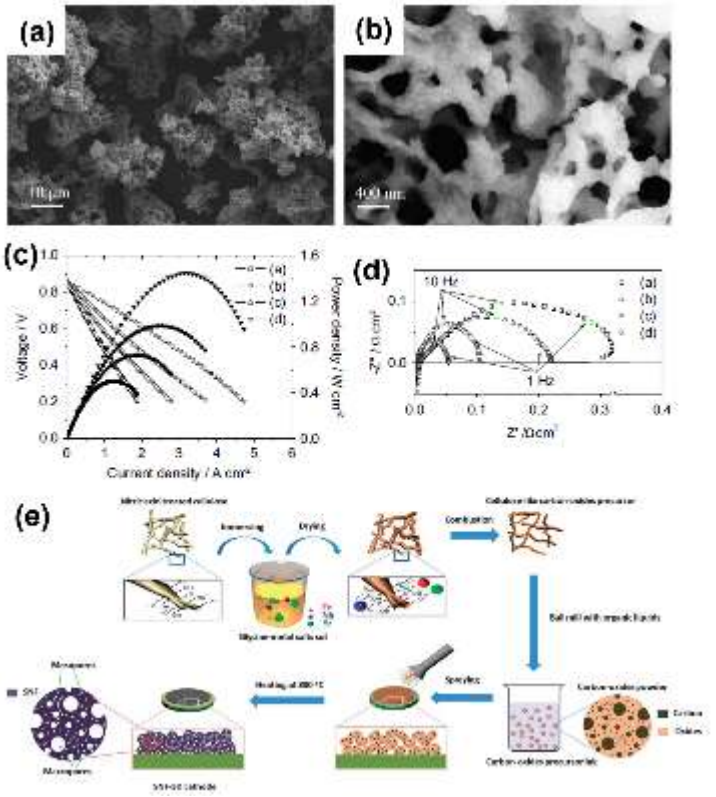

Figure 9. **(a**, **b)** SEM images at low **(a)** and high **(b)** magnification. **(c)** Typical I-V-P curves and **(d)** electrochemical impedance spectra of the cells with four types of SSC-GDC cathodes obtained from (a) TC (traditional-combustion without glycine), (b) TC-G (traditional-combustion with glycine), (c) FC (freeze-drying combustion without glycine), and (d) FC-G (freeze-drying combustion with glycine) routes, respectively, operating at 600 °C. Reproduced with permission.[182] Copyright 2014, Elsevier. **(e)** Preparation route for a 3D hierarchical porous $SrNb_{0.1}Fe_{0.9}O_{3-\delta}$ (SNF-3D) cathode. Reproduced with permission.[66] Copyright 2012, Royal Society of Chemistry.

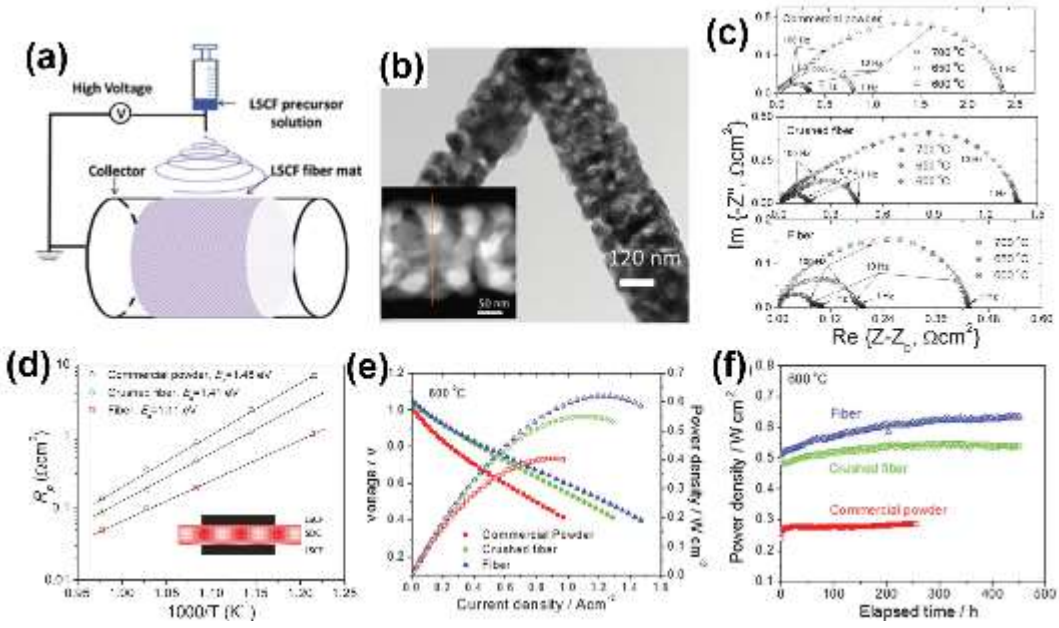

Figure 10. **(a)** A schematic displaying the electrospinning process for the construction of nanofibers. **(b)** TEM and Scanning TEM (STEM) (inset) images of the as-made LSCF fibers. **(c)** Electrochemical impedance

spectra curves at different temperatures (600, 650, and 700 °C) for the cells with different LSCF cathodes made from commercial LSCF powder (top), crushed LSCF fibers (middle), and well-grown LSCF fibers (bottom), respectively, under open circuit voltage conditions. **(d)** Dependence of interfacial polarization resistances (R_p) on the operating temperatures for three electrodes of commercial LSCF powder, crushed LSCF fibers, and well-grown LSCF fibers, obtained from the data in (c). **(e)** I-V-P curves and **(f)** long-term stability measurement at a fixed potential of 0.7 V for the cells with commercial LSCF powder, crushed LSCF fibers, and well-grown LSCF fibers as cathodes, respectively, operating at the temperature of 600 °C and employing humidified H_2 (3% H_2O) as fuel and ambient air as oxidant. Reproduced with permission.[183] Copyright 2017, Wiley-VCH.

Besides, analogously, several porous perovskites are also employed as anodic catalysts to facilitate fuel oxidation. Song and his co-workers proposed a novel composite anode with a hierarchically porous framework and comprising water-storable $BaZr_{0.4}Ce_{0.4}Y_{0.2}O_{3-\delta}$ perovskite, amorphous BaO, and Ni nanoparticles, for operating in SOFCs with H_2S-containing mixed gas as fuels. [186] Such structured composite anode was synthesized via infiltrating a liquid precursor that had a nominal $Ba(Zr_{0.4}Ce_{0.4}Y_{0.2})_{0.8}Ni_{0.2}O_{3-\delta}$ composition into the porous $Sm_{0.2}Ce_{0.8}O_{1.9}$ (SDC) scaffold, followed by calcination and reduction under H_2 atmosphere. The electrochemical testing found that relative to a conventional anode of Ni+SDC, such architecture offered a more exceptional electrochemical H_2-oxidation activity, higher sulfur tolerance, and more remarkable working stability, even with the blended 1000 ppm H_2S-H_2 fuel.

Other than utilization as electrodes in SOFCs, as well, porous perovskites $LaNiO_3$ cubes were also reported as the support of Pt nanoparticles for direct methanol fuel cells. [187] In this work, porous $LaNiO_3$ nanocubes were prepared by a facile hydrothermal strategy with $La(NO_3)_3 \cdot 6H_2O$, $Ni(NO_3)_2 \cdot 6H_2O$, glycine, and PVP as raw materials (**Figure 11a**), where the roles of these chemical reagents have been discussed above. After a thermal treatment at 400 °C for 2 h, the distinct porous nanocubes with an edge length of 300-400 nm was obtained as shown in **Figure 11b** and **c**, which demonstrated a high BET specific surface area of 65 m^2g^{-1} and a large average pore diameter of about 9.5 nm. Then, by further reducing H_2PtCl_6 with $NaBH_4$ at room temperature in the solution, the ultrafine Pt nanoparticles (about 5 nm) resided in the pore channels of porous $LaNiO_3$. When evaluated as the catalysts toward methanol oxidation in both acidic and alkaline solutions, the as-obtained Pt/$LaNiO_3$ hybrid demonstrated superior activity to that of Pt/C or pure Pt nanoparticles (**Figure 11d** and **e**), particularly giving an obvious negative shift toward onset potential of 0.1 and 0.23 V in 0.1 M H_2SO_4 electrolyte. Herein, of note, the porosity can strengthen the distribution degree of the Pt nanoparticles and mass transfer of the reactants and products. In addition, these inner pores made the methanol molecules stay longer, so that they can be oxidized sufficiently in case to form the poison product CO.

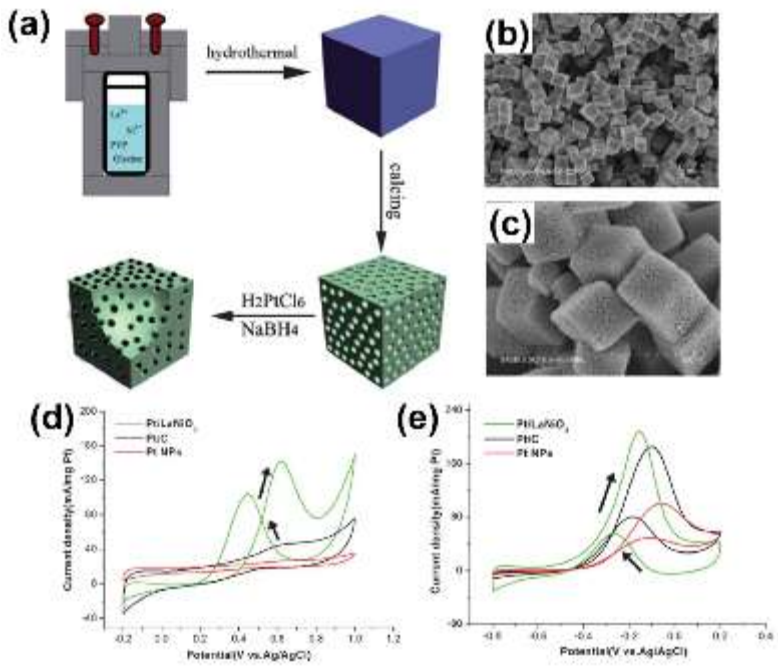

Figure 11. **(a)** Procedure for the synthesis of porous $LaNiO_3$ nanocubes and loading Pt nanoparticles on them. **(b**, **c)** SEM images of the porous $LaNiO_3$ nanocubes. **(d**, **e)** Cyclic voltammetry curves of as-obtained Pt/$LaNiO_3$ hybrid, Pt/C and pure Pt nanoparticles in the acidic (1.0 M CH_3OH+0.1 M H_2SO_4) (d) and alkaline (1.0 M CH_3OH+0.1 M KOH) media (e). Reproduced with permission.[187] Copyright 2012, Royal Society of Chemistry.

4.1. Metal-air batteries

In virtue of their high energy densities, cheap production costs, along with the environmental-friendly operation, metal-air batteries, as another kind of highly efficient intermediate device for energy storage and conversion, have garnered widespread attention in recent years. Particularly, in comparison with that of commercially used Li-ion batteries, a leap forward for the specific energy in metal-air batteries is observed, increasing from 387 to about 3500 Wh kg^{-1}. [188] Normally, the metal-air battery systems are made up of an air cathode, an electrolyte, and an active metal anode including Li, Na, Ca, Mg, Zn, and Al, etc. [53] At their cathode, oxygen (O_2) is reduced during discharge (ORR), and in inverse O_2 is produced (OER) during charge. At their anode, the metal and metal ions undergo oxidation and reduction reactions during discharge and charge, respectively. Although with multifarious metal electrodes, only Li and Zn metals corresponding to constitute Li-air batteries and Zn-air batteries, denoted as LABs and ZABs, respectively, have aroused the broadest enthusiasm among researchers. [163, 189] In such two metal-air batteries, the fundamentally overall reactions are described as below: $Li + O_2 \leftrightarrow Li_2O_2$ and $Zn + O_2 \leftrightarrow ZnO$, respectively, along with the desired half -cell reaction at the cathode of $O_2 + 2Li^+ + 2e^- \leftrightarrow Li_2O_2$ and $O_2 + 2H_2O + 4e^- \leftrightarrow 4OH^-$, respectively. During the discharge process, Li_2O_2 and ZnO are regarded as the most common solid products in the LABs and ZABs, respectively. On account of the relatively sluggish kinetics of oxygen electrocatalysis at the cathode, efficient electrocatalysts should be needed to endow the air electrode with a high electrocatalytic behavior, so as to promote the discharge/charge process

and enhance the total energy efficiency. According to numerous previous reports, it is a consensus that perovskite-type electrode materials are ideally suited to improve the electrochemical performance of LABs and ZABs.[163, 190] Nevertheless, traditionally synthesized perovskites normally show a featureless micro-morphology with the large particle size, and the nearly porosity-free structure, thus which would bring about limited catalytic effectiveness. To tackle this issue, porous nano-architecture engineering appears to be a feasible approach.

Porous perovskite oxides applied in the air electrode of Li-air batteries have been extensively studied in recent years. [59, 60, 64, 123, 137, 146, 148, 191-199] For instance, in 2014, Zhang et al. synthesized the porous perovskite $LaNiO_3$ nanocubes as cathode catalysts for Li-air batteries, where the modified hydrothermal process was used with glycine as the shape-control and pore-creating agent. [123] After annealing in O_2 at 650 ^oC for 2 h, the resulting porous $LaNiO_3$ nanocubes have an average pore diameter of about 30 nm, and the corresponding BET specific surface area was around 36 $m^2\ g^{-1}$. With the aid of such obtained porous $LaNiO_3$ catalysts, the battery displayed excellent charging properties with the significantly decreased overpotential (3.40 V) and offered a much improved capacity of 3407 mAh g^{-1} in comparison with that of the bulk counterpart. In addition, excellent cycle stability (~75 cycles) with any unobvious capacity attenuation was evidenced at a 500 mA h g^{-1} capacity limitation. On basis of physical characterizations, it was also found that the lithium anode corrosion to form LiOH coating and cathode passivation from the blocking of grown Li_2CO_3 should be responsible for the capacity fading in Li-air batteries. Ju and his co-workers employed PMMA as the hard templates to prepare a $Nd_{0.7}Sr_{0.3}CoO_{3-\delta}$ perovskite with 3D ordered mesoporous framework (3DOM-NSC) and compared the performance with the benchmark Pt/C and pure carbon black. [194] As displayed in **Figure 12a**, a honeycomb-like pore structure in three dimensions was successfully formed after eliminating templates upon annealing, which was composed of well-dispersed "air spheres" and interconnected walls. Such morphology created a high surface area of nearly 22 $m^2\ g^{-1}$. When maintaining a current density of 0.5 mA cm^{-2}, 3DOM-NSC presented an obvious higher discharge voltage platform and lower charge voltage platform than that of pure carbon (**Figure 12b**). Additionally, although the discharge voltage of a battery with the benchmark Pt/C electrode was slightly higher than that of 3DOM-NSC, the charge voltage on the cells with 3DOM-NSC was lower than that of the Pt/C (**Figure 12b**). After a continuous 40-h cycling operation (about 20 cycles) at a fixed current density of 0.1 mA cm^{-2}, almost no degradation was observable, as shown in **Figure 12c**. Later, on basis of a modified reflux method via adopting carbon nanospheres as the pore-creating material, the well-developed hollow and porous structured $La_{0.6}Sr_{0.4}CoO_{3-\delta}$ spheres (HS-LSC) were successfully fabricated by Lee's group. [59] In this synthesis, carbon nanospheres were first achieved from a hydrothermal-processed glucose solution. $La(NO_3)_3{\cdot}6H_2O$, $Sr(NO_3)_2$, and $Co(NO_3)_3{\cdot}6H_2O$ were chosen as metal raw materials, as well as urea as the complexing agent. When they mixed with the carbon nanospheres in a certain water solution, the resulting mixture then was refluxed for 5 h at 120 °C, followed by further calcination (HS-LSC-10, corresponding to the pyrolysis temperature of 1000 °C). As a result, owing to the favorable morphological features for ion/gas/electrolyte transport, it was evident that the efficient bifunctional catalytic performance toward ORR and OER with smaller polarization of HS-LSC-10 is registered (**Figure 12d** and **e**), which eventually boosted the energy output with a deep discharge capacity of 4895 mA h

g^{-1} and a round-trip efficiency (~82%) in reduction and oxidation processes relative to that of the particulate structure (NP-LSC-10) in the LAB assembly (**Figure 12f**). Similarly, $La_{0.5}Sr_{0.5}CoO_{3-x}$ perovskite nanotubes owning hierarchical mesoporous/macroporous structure was also designed by Liu and his co-workers with the electrospinning technique, as shown in **Figure 13** and offered a distinguished performance for both discharge and charge processes in Li-O_2 cells. [197] Moreover, the synergy of hierarchical porous architecture and outstanding catalytic activity led to excellent rate capability and good cyclability with a controlled specific capacity of 500 mA h g^{-1} at a fixed current density of 0.1 mA cm^{-2}.

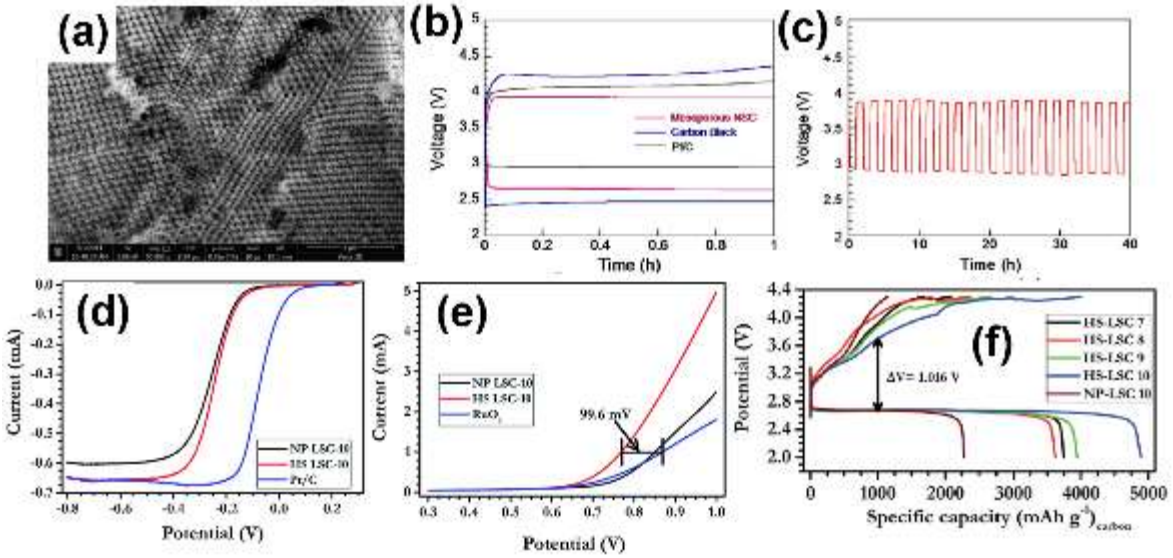

Figure 12. **(a)** SEM image of 3DOM-structured $Nd_{0.7}Sr_{0.3}CoO_{3-\delta}$. **(b)** The first discharge-charge curves at a fixed current density of 0.5 mA cm^{-2} in the LAB assembly with 3DOM-NSC, Carbon black, and Pt/C as air electrodes, respectively. **(c)** Galvanostatic discharge-charge cycling curves of Li-air batteries using the 3DOM-NSC air electrode and with a 2-h long interval cycle at a current density of 0.1 mA cm^{-2}. Reproduced with permission.[194] Copyright 2015, The Electrochemical Society. **(d)** ORR and **(e)** OER polarization curves of NP LSC-10, HS-LSC-10, and commercial Pt/C samples in O_2-saturated 0.1 M KOH aqueous solution at the rotating speed of 1600 rpm. **(f)** The first discharge-charge profiles of all HS-LSC materials and NP-LSC-10 at a constant current rate of 0.1 A g^{-1}. Reproduced with permission.[59] Copyright 2017, Royal Society of Chemistry.

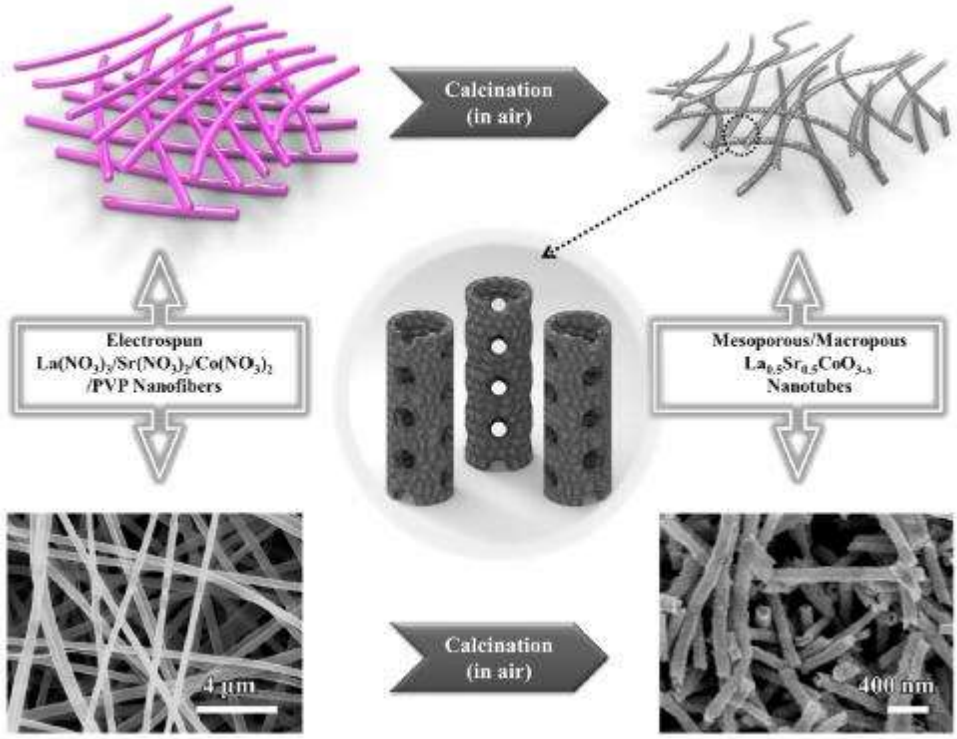

Figure 13. Schematic diagram depicting the fabrication of $La_{0.5}Sr_{0.5}CoO_{3-x}$ perovskite nanotubes with hierarchical mesoporous/macroporous architecture. Reproduced with permission.[197] Copyright 2015, American Chemical Society.

Apart from these, several other similar perovskite oxides, such as porous $CaMnO_3$ nanoparticles obtained by a sol-gel complexing route, [60] 1D porous $La_{0.75}Sr_{0.25}MnO_3$ or $La_{0.5}Sr_{0.5}CoO_{2.91}$ nanotubes prepared via the electrospinning technique, [146, 196] and 3DOM structured $LaFeO_3$ or $La_{0.6}Sr_{0.4}CoO_{3-\delta}$ based on a PMMA hard-templating method, [193, 195] etc. were also demonstrated to offer large capacity, excellent rate capability, and robust cycle stability when used as catalysts in the air electrode of LABs. Furthermore, given the insufficient electrical conductivity in perovskite-type oxides, modification of oxides with carbon-based nanomaterials is considered as one significantly feasible strategy to optimize the catalytic behavior in LABs. [137, 191, 192] According to the aforementioned report by Yang et al., the as-prepared G/meso-LaSrMnO hybrid with unique architecture was directly served as the freestanding air electrode for LABs with lithium bis (trifluoromethanesulfonyl) imide (LiTFSI) dissolved in tetraethylene glycol dimethyl ether (TEGDME) as electrolyte, which presented a large discharge voltage plateaus of 2.77 V (vs. Li^+/Li) and a high specific capacity of 21470 mAh g^{-1} at a current density of 100 mA g^{-1} with respect to the LaSrMnO catalyst loading. [137] In addition, the G/meso-LaSrMnO electrode displayed outstanding cyclic stability up to 50 cycles and a high Coulombic efficiency of almost 100 %. The study revealed that the volume change rooting from the generation and decomposition of Li_2O_2 during the discharge/charge process could be well accommodated by the hierarchical porous and flexible composite structure in the air electrode, thus leading to such excellent catalytic properties. To further verify the advantages of the metal oxide-carbon composites, a similar hybrid of porous $La_{0.8}Sr_{0.2}MnO_3$ nanocrystals uniformly supported on N-doped graphene (named as LSM/NrGO), that was produced by a simple electrostatic adsorption-hydrothermal-calcination

joint process, was also tested in the Li-O_2 cell by Chen et al. [192] They found that relative to bare $La_{0.8}Sr_{0.2}MnO_3$, addition of NrGO might effectively lower the polarization and obtain more remarkable bifunctional catalytic behaviors, especially for the ORR. Therefore, a higher specific capacity value, more stable discharge voltage, and superior rate capability were realized in the batteries with the LSM/NrGO catalyst.

Recently, several researchers proposed that the RuO_2 material may be another component to produce hybrids with porous perovskite. [198, 199] Zhang et al. created a novel composite of porous $La_{0.6}Sr_{0.4}Co_{0.8}Mn_{0.2}O_3$ (LSCM) nanofibers coated with numerous RuO_2 nanosheets as a catalyst in LABs, which was denoted as RuO_2@LSCM NFs. [199] During the synthesis as shown in **Figure 14a**, the nanofiber-structured LSCM was first gained by employing an electrospinning-calcination approach and then a wet impregnation route was adopted to attach RuO_2 nanosheets to the surface of LSCM nanofibers. The as-electrospun LSCM nanofibers had a slight shrinkage in the diameter of 200-300 nm, with a huge quantity of small pores formed on the wall (**Figure 14b**). The loaded RuO_2 nanosheets showed an ultrathin thickness of ~ 10 nm (**Figure 14c**). Moreover, the BET specific surface area and average pore diameter of RuO_2@LSCM NFs was 50.88 m^2 g^{-1} and 38.9 nm, respectively, which were much larger than the results in pure LSCM nanofibers (17.5 m^2 g^{-1} and 22.6 m, respectively.). Such a unique porous composite architecture favored the contact between electrolyte and electrode, promoted O_2 diffusion, offered abundant active sites, and enhanced the conductivity. At the same time, the synergy of LSCM and RuO_2 not only facilitated the decomposition of both lithium carbonate and lithium hydroxide, but also improved both ORR and OER catalytic behavior. All of these factors made RuO_2@LSCM NFs better than pure LSCM nanofibers and stood out among other catalysts toward rechargeable LABs and displayed a high initial discharge capacity of about 12742 mA h g^{-1}, low voltage range from 2.6 to 4.3 V, as well as good cyclability (≥100 cycles), as shown in **Figure 14d-f**.

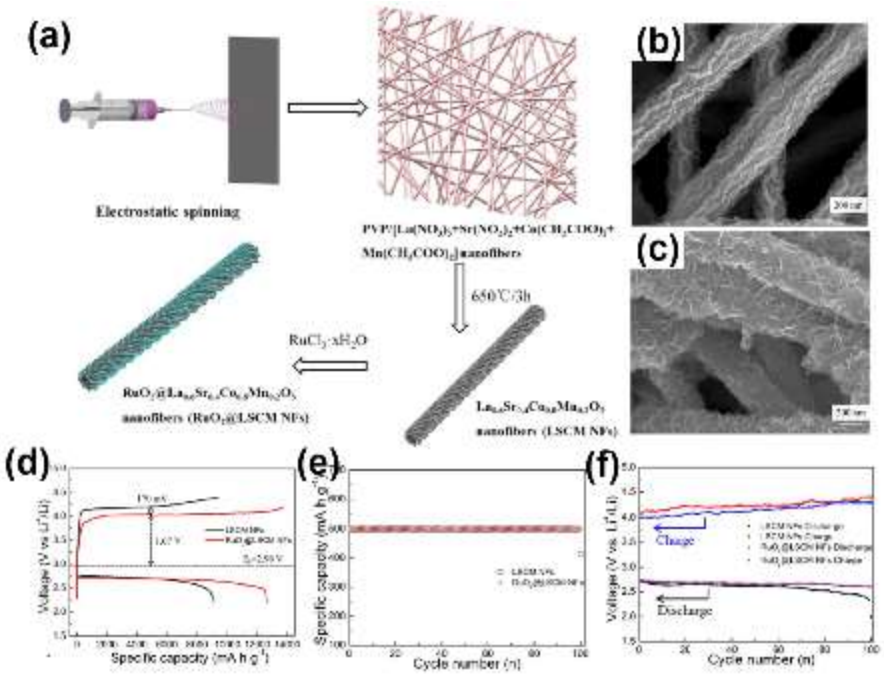

Figure 14. **(a)** A schematic illustrating the synthetic strategy of LSCM NFs and RuO_2@LSCM NFs. **(b**, **c)** Typical SEM images of LSCM NFs **(b)** and RuO_2@LSCM NFs **(c)** catalysts. **(d)** 1st discharge/charge curves, **(e)** cycling performance, and **(f)** discharge/charge terminal voltages of Li-air cells based on LSCM NFs and RuO_2@LSCM NFs cathodes at a fixed current density of 50 mA g^{-1}. Reproduced with permission.[199] Copyright 2017, American Chemical Society.

Besides, lately, there is also a large upsurge of interest in Zn-air batteries, and perovskites with various porous nanostructures have appeared to be promising catalytic materials on the air electrode. [56, 58, 61, 62, 70, 124, 126-128, 200-202] Sun et al., by using PMMA hard templates, synthesized 3D ordered porous Ag-doped $LaFeO_3$ (LFA) as a remarkable ORR electrocatalyst in alkaline media. [56] The hierarchically porous structure for this material led to a high BET specific surface area and large pore volumes for mass/ions diffusion, eventually contributing to significantly boosted ORR performances relative to the LFA nanoparticles. Thus, it might display promise in the application of ZABs. Vignesh and his co-workers reported the electrospun preparation of Ni-doped $LaCo_{0.96}O_{3-\delta}$($La(Co_{0.71}Ni_{0.25})_{0.96}O_{3-\delta}$) with a uniform morphology of porous nanotubes (**Figure 15a**). [124] Its performance in ZABs were then elucidated in 6 M KOH solution (**Figure 15b**). As expected, by taking merits of the special porous tube-like micro/nano-structure and collaborative influence between Ni and Co, the as-prepared $La(Co_{0.71}Ni_{0.25})_{0.96}O_{3-\delta}$ material exhibited superior catalytic behavior to the corresponding binary and bulk counterparts. In the primary battery, a specific discharge capacity for this $La(Co_{0.71}Ni_{0.25})_{0.96}O_{3-\delta}$ sample was 705 mAh g_{zinc}^{-1}, corresponding to a specific energy output of about 846 mWh g_{zinc}^{-1}, which was higher than these results observed for the porous $LaCo_{0.97}O_{3-\delta}$ and bulk $LaCo_{0.75}Ni_{0.25}O_{3-\delta}$ catalysts **(Figure 15c**). When applying it in rechargeable ZABs, with a fixed current density of 5 A g^{-1}, the porous $La(Co_{0.71}Ni_{0.25})_{0.96}O_{3-\delta}$ nanotubes yielded a smaller potential gap of 0.529 and 0.792 V for the 1st and 20th cycle, respectively, compared with the $LaCo_{0.97}O_{3-\delta}$ and benchmark Pt/C catalysts (**Figure 15d-f**). Similarly, Kim's group also fabricated porous nanofiber-structured $PrBa_{0.5}Sr_{0.5}Co_{1.5}Fe_{0.5}O_{5+\delta}$ perovskite through an electrospinning technique, and demonstrated a distinguished discharge capacity and good charge-discharge cycling stability, comparable to the contrast sample Pt/C+IrO_2. [61] Analogous to the usage of perovskite oxides in LABs, hybridizing with various carbons by in situ synthesis is a good choice to enhance the electrical conductivity of perovskite oxides. For example, a combination of $BaMnO_3$ porous nanorods and a thin carbon layer through a hydrothermal method produced remarkably improved OER/ORR activity and stability in comparison with bare $BaMnO_3$ nanorods. [58] As well, Thanh and his workers reported the usage of a novel composite nanomaterial based on porous hollow $LaNiO_3$ spheres monodispersedly anchored on N, S-codoped graphene ($LaNiO_3$/N,S-Gr) for boosting ORR performance in the alkaline electrolytes (**Figure 16b**). [126] The fabrication process for the $LaNiO_3$/N,S-Gr composite was schematically given in **Figure 16a**, which mainly involved the hydrothermal route and subsequent calcination. With the hybridization with the heteroatoms-doped graphene, the onset and half-wave potential of the $LaNiO_3$/N,S-Gr nanohybrid positively shifted to -0.05 and -0.18 V, respectively, as compared to separate $LaNiO_3$ spheres with porous and hollow structure, which was -0.08 and -0.19 V, respectively. Such enhancement could be attributed to two facts: one is that the synergistic effect created between porous hollow $LaNiO_3$ nanospheres and heteroatom doping influence on the graphene led to more active sites and improved interactions; The other is that the presence of N,S-Gr enhanced the electrical

conductivity and arouse excellent dispersion of perovskite species on the surface of graphene. These results shed light on the significant potential application of the carbon-hybridized porous perovskite on ZABs. Besides, Shanmugam's group *in-situ* introduced N-doped carbon on $LaTi_{0.65}Fe_{0.35}O_{3-\delta}$ particles to form 1D porous nanorods (LTFO-C) by the electrospinning route and subsequent annealing in Ar-saturated atmosphere (**Figure 16c**). [128] Such hybrids showed a specific surface area about 14 times higher than that of separate $LaTi_{0.65}Fe_{0.35}O_{3-\delta}$ nanotubes obtained by annealing in the air (204 vs 15 m^2 g^{-1}). Shown in **Figure 16d** and **e** was the tested electrochemical performance in a Zn-air battery. At a fixed current density of 5 A g^{-1}, the LTFO-C presented extraordinarily smaller charge-discharge potential gap than pure 1D $LaTi_{0.65}Fe_{0.35}O_{3-\delta}$ nanotubes (LTFO-B) and N-doped carbon nanorods (NCNR) over 60 charge-discharge cycles. A slight increase of this gap from 0.57 to 0.83 V was observed for the LTFO-C composite in the first and sixtieth cycle. In sharp contrast, the LTFO-B exhibited a significant leap of the potential gap from 0.81 V to 1.46 V, which suggested an enhanced stability and reversibility after hybridizing with carbon.

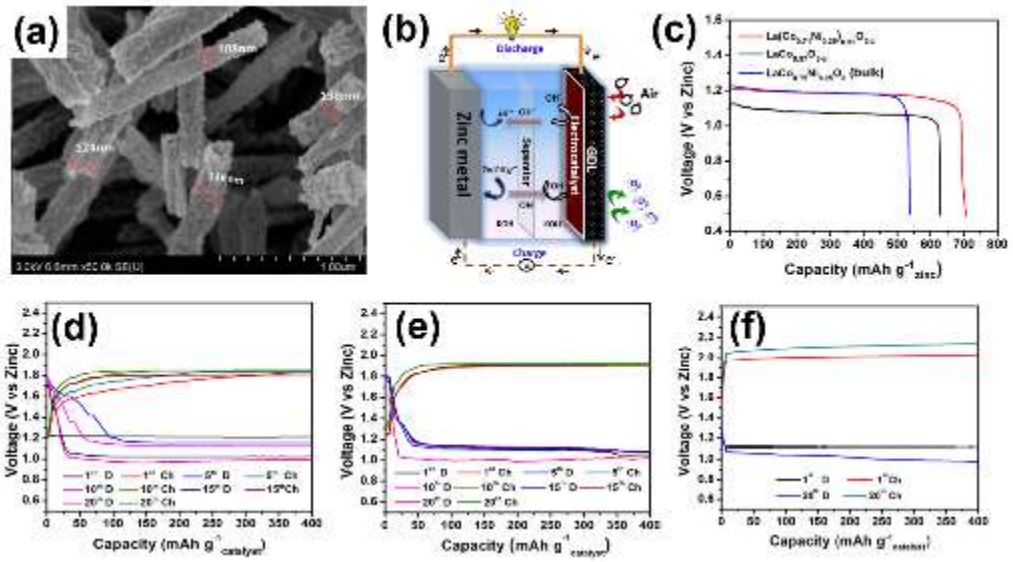

Figure 15. **(a)** Typical SEM image of porous $La(Co_{0.71}Ni_{0.25})_{0.96}O_{3-\delta}$ nanotubes prepared by an electrospining method. **(b)** The schematic description of rechargeable Zn-air batteries. **(c)** Discharge curves of primary ZABs with varied catalysts at a 5 A g^{-1} current rate and on basis of consumption of Zn anode. **(d-f)** Galvanostatic discharge (D)-charge (Ch) profiles of rechargeable ZABs using different air electrodes at a fixed current density of 5 A g^{-1} with a limited capacity of 400 mA h $g_{catalyst}^{-1}$. **(d)** $La(Co_{0.71}Ni_{0.25})_{0.96}O_{3-\delta}$; **(e)** $LaCo_{0.97}O_{3-\delta}$; **(f)** commercial 20 wt % Pt/C. Reproduced with permission.[124] Copyright 2016, American Chemical Society.

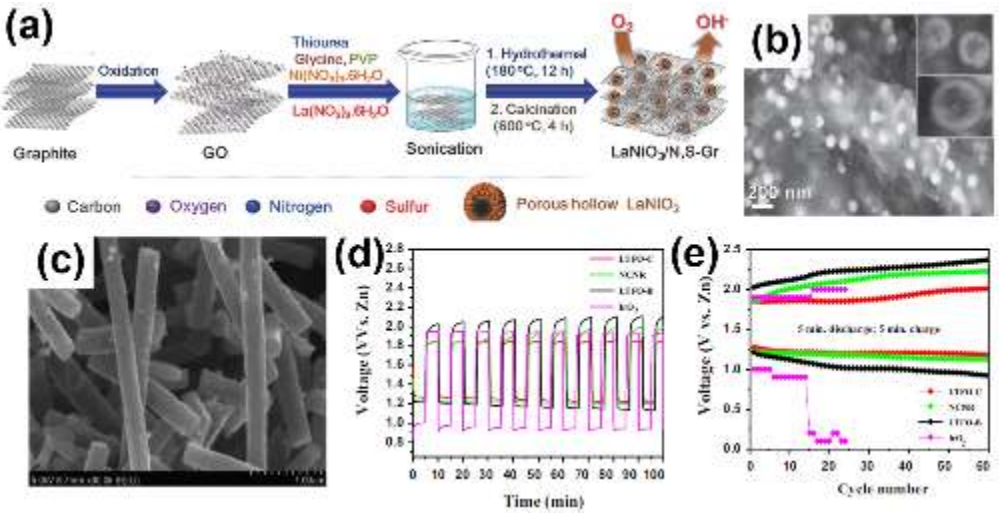

Figure 16. **(a)** A Schematic to illustrate the growing route of the $LaNiO_3$/N,S-Gr nanohybrid. **(b)** Low- and high- (Inset) magnification SEM images of the $LaNiO_3$/N,S-Gr nanohybrid. Reproduced with permission.[126] Copyright 2017, Wiley-VCH. **(c)** Representative SEM image of LTFO-C showing 1D porous nanorods. **(d)** Galvanostatic discharge-charge cycling curves and **(e)** discharge/charge terminal potentials at a current density of 5 A g^{-1} with the cycle interval of 10 min for Zn-air cells based on LTFO-C, NCNR, LTFO-B, and IrO_2 cathode catalysts. Reproduced with permission.[128] Copyright 2015, Elsevier.

Aside from the LABs and ZABs, perovskite oxides equipped with large surface area and rich porosity are used in other metal-air batteries as well. Hu et al. developed a porous microsphere structured $CaMnO_3$ material via the simple pyrolysis of a solid-solution precursor, $CaMn(CO_3)_2$ and employed it as a cathodic electrocatalyst in rechargeable sodium-oxygen (Na-O_2) batteries. [203] The porous architecture was well created through interconnected $CaMnO_3$ nanoparticles, giving a high surface area up to 11.8 m^2 g^{-1}. Such $CaMnO_3$/C cathode offered a high capacity of 9560 mA h g^{-1} at a constant current density of 100 mA g^{-1}, much higher than that of carbon-only electrode (3870 mA h g^{-1}). When fixing the capacity at 1000 mA h g^{-1}, the $CaMnO_3$/C electrode maintained outstanding cyclability without any degradation after 80 cycles, which is extremely better than that of the pure carbon cathode (< 10 cycles). The excellent performance might be ascribed to porous micro-nano framework in $CaMnO_3$ microspheres, which afforded rich active sites toward ORR/OER and effective room for the product accommodation. These exemplified results highlighted the promising application of the porous perovskites in various metal-air batteries.

5 Summary and Outlook

Here, we reviewed the substantial advances of porous perovskite-based materials as electrocatalysts applied in various practical energy-related devices, such as metal-air batteries and fuel cells, as shown in **Table 1**. The construction of porous architecture in perovskite oxides is viable through mastering various advanced preparation strategies with controllable synthetic conditions, which involve HEBM-assisted or molten salts-incorporated solid-state, sol-gel complexation, combustion, hydrothermal, electrospinning routes, etc., with sometimes introducing surfactant and/or template additives, and several featured nanostructures of nanorods, nanowires, nanocubes, nanospheres, and 3DOM honeycomb-like morphology, etc., was easily achieved under some such routes. Obviously noting, porous nanostructures not only

endow these perovskite-based materials with large surface area and sufficient pore volume, but also offer more gas/ion transfer channels and expose richer active sites for catalytic reactions. Therefore, these nanostructured perovskites with favorable porosity has proved to possess excellent electrocatalytic activity for fundamental fuel oxidation reactions, ORR, and OER in the anode or cathode of fuel cells and the air electrode of metal-air batteries, which outperform the bulk counterpart attained from conventional methods and even are better than the commercial noble metal benchmark. Although recent years witness the great research progresses in the development of porous perovskite nanostructures for various energy-related applications, it still sites at a nascent stage, and much more room could be flourished for the field. Several specific aspects needing more attention are shown as below.

(1) The well phase formation of perovskite-related materials by universal approaches usually requires high sintering temperature, contributing to the small surface area and insufficient porosity. Although several reported novel strategies or modified traditional methods, like hydrothermal, electrospinning, molten salts-incorporated solid-state, and template-involved sol-gel synthesis, etc. have significantly lowered the synthetic temperature and realized porous nanostructure, just a few simple perovskites could be successfully achieved via them, which is not universal. Besides, the precise control of pore size is still a challenging issue. Therefore, future studies are expected to explore more perovskite nanostructures with the tunable pore channels by these adjusted synthetic protocols or exploiting more advanced fabrication techniques to obtain these target products.

(2) As to perovskite oxides, the poor electrical conductivity still becomes a critical factor that limits their electrocatalytic activity in various energy-related devices. Complex catalysts, combining perovskite oxides with another conductive phase such as metal or functional carbon is deemed to attain a promising alternative. More importantly, a synergy can be generated between different phases, which will promote the charge transfer and thus improve the energy-exchange efficiency. For compositing perovskites with a conductive material, the potential reaction between perovskites and the second phase needs well attention since perovskite is easy to react with a reducant agent while conductive carbon and metals are usually reducing materials.

(3) In addition to morphology, the electrocatalytic behavior of metal oxides has a large dependence on their electronic structure, which can be manipulated by tuning chemical composition, and doping aliovalent ions. Previous studies have pointed out that the transition metals in octahedron with an e_g filling close to 1 afforded a high OER and ORR electrocatalytic activity. Accordingly, electronic structure engineering should be taken into account in elaborately fabricating their porous architecture, for instance, cobalt, nickel, and manganese with trivalent state having an intermediate-spin state.

(4) Different from the fundamental study for the half reaction such as OER, ORR, and HER in alkaline aqueous solutions, the real-world energy devices present more complicated reactions process. For example, Li_2O_2 or ZnO is formed as common solid products during the discharge process in the LABs or ZABs, respectively, which could significantly affect the efficiency of the reverse process. Consequently, in such devices such as metal-air batteries or fuel cells, it is significant yet still highly challenging to well understand the underlying catalytic mechanism, since it needs to disclose how the interaction between different components can enhance the efficiency of catalysts. In this regard, advanced characterization techniques including Operando X-ray absorption spectroscopy (XAFS), in-situ XRD, Raman, and TEM, etc. is

expected to be applied in the study of these devices, so as to offer atomic-level insights into the changes of the anodic or cathodic electrode in different cells. Meanwhile, modeling simulations should be required to help a better understanding of the effect of realistic operational conditions on the overall performance of the devices with porous perovskite electrodes.

(5) The stability issues of the electrode catalyst deserve further investigation, as the long-term working is a prerequisite for practical implications. In the case of metal-air batteries, only several hundreds of charge-discharge cycles could be maintained. In fact, many perovskite oxides are not stable in aqueous solutions, the leaching of compositional elements into the electrolyte could be happened, which can be further strengthened under electric force. On the basis of these, multiple above-mentioned novel techniques need to be employed to ensure an in-depth understanding of the poor stability and so a scientific guideline will be defined for the exploration of more stable perovskite-based nanomaterials.

(6) Moving forward, apart from some technical issues involved between fundamental study and industrial application, the cost of the raw materials and the accessibility of the synthetic route of electrocatalysts, etc., also largely restrict the large-scale industrial implementation of these perovskite electrocatalysts, which must be tackled.

To sum up, with the continuous study in this trend by our group and plenty of others worldwide, more surprising possibilities will take place.

Table 1 Summary of porous perovskite nanostructures obtained by various routes for these applications of fuel cells and metal-air batteries.

Perovskites	Morphology	Synthesis	Templates	Applications	References
$Sm_{0.5}Sr_{0.5}CoO_{3-\delta}$-SDC	Porous nano-network	Infiltration	Without	SOFCs	[178]
$Sm_{0.5}Sr_{0.5}CoO_{3-\delta}$-GDC	Porous nano-network	Vacuum-free infiltration and freeze-drying combustion	Without	SOFCs	[182]
$SrNb_{0.1}Fe_{0.9}O_{3-\delta}$	Porous nanoparticle	Solution combustion	cellulose-like carbon	SOFCs	[66]
$La_{0.6}Sr_{0.4}Co_{0.2}Fe_{0.8}O_{3+\delta}$	Porous nanofibers	electrospinning	Without	SOFCs	[183]
$(PrBa)_{0.95}(Fe_{0.9}Mo_{0.1})_2O_{5-\delta}$	Porous nanoparticle	Sol-gel	Without	SOFCs	[184]
$BaZr_{0.4}Ce_{0.4}Y_{0.2}O_{3-\delta}$-BaO-Ni	Porous nano-network	Infiltration	Without	SOFCs	[186]
$LaNiO_3$	Porous cubes	Hydrothermal	Without	DMFCs	[187]
$LaNiO_3$	Porous cubes	Hydrothermal	Without	LABs	[123]
$Nd_{0.7}Sr_{0.3}CoO_{3-\delta}$	3DOM	Template-assisted	PMMA	LABs	[194]
$La_{0.6}Sr_{0.4}CoO_{3-\delta}$	Hollow porous spheres	Reflux	Carbon nanospheres	LABs	[59]
$La_{0.5}Sr_{0.5}CoO_{3-\delta}$	Porous nanotubes	Electrospinning	Without	LABs	[197]
$CaMnO_3$	Porous nanoparticles	Sol-gel	Without	LABs	[60]
$LaFeO_3$	3DOM	Template-assisted	PMMA	LABs	[193]
$La_{0.8}Sr_{0.2}MnO_3$/NrGO	Porous composite	Hydrothermal	Without	LABs	[192]
RuO_2@$La_{0.6}Sr_{0.4}Co_{0.8}Mn_{0.2}O_3$	Porous composite	Electrospinning-impregnation	Without	LABs	[199]
Ag-doped $LaFeO_3$	3DOM	Template-assisted	PMMA	ZABs	[56]
$La(Co_{0.71}Ni_{0.25})_{0.96}O_{3-\delta}$	Porous nanotubes	Electrospinning	Without	ZABs	[124]
$PrBa_{0.5}Sr_{0.5}Co_{1.5}Fe_{0.5}O_{5+\delta}$	Porous nanofiber	Electrospinning	Without	ZABs	[61]
$BaMnO_3$@ carbon layer	Porous nanorods	Hydrothermal	Without	ZABs	[58]
$LaNiO_3$/N,S-Gr	Porous hollow $LaNiO_3$ spheres	Hydrothermal	Without	ZABs	[126]
$LaTi_{0.65}Fe_{0.35}O_{3-\delta}$-C	Porous nanorods	Electrospinning	Without	ZABs	[128]
$CaMnO_3$	Porous microsphere	Pyrolysis	Without	Na-O_2	[203]

References

1. M. Winter, R. J. Brodd, *Chem. Rev.* **2004**, *104*, 4245.
2. M. A. Rahman, X. J. Wang, C. E. Wen, *J. Electrochem. Soc.* **2013**, *160*, A1759.
3. M. Du, K. Liao, Q. Lu, Z. Shao, *Energy Environ. Sci.* **2019**, *12*, 1780.
4. Z. P. Shao, S. M. Haile, *Nature* **2004**, *431*, 170.
5. L. K. Wang, Y. C. Zhou, J. Timoshenko, S. Z. Liu, Q. Qiao, K. Kisslinger, M. Cuiffo, Y. C. Chuang, X. H. Zuo, Y. Xue, Y. C. Guo, C. Pan, H. F. Li, C. Y. Nam, S. Bliznakov, P. Liu, A. I. Frenkel, Y. M. Zhu, M. H. Rafailovich, *ACS Catal.* **2019**, *9*, 1446.
6. S. Weitemeyer, D. Kleinhans, T. Vogt, C. Agert, *Renew. Energy* **2015**, *75*, 14.
7. W. Wang, X. M. Xu, W. Zhou, Z. P. Shao, *Adv. Sci.* **2017**, *4*, 1600371.
8. M. Q. Ren, J. B. Zhang, M. M. Fan, P. M. Ajayan, J. M. Tour, *Adv. Mater. Interfaces* **2019**, *6*, 1901035.
9. P. Tan, B. Chen, H. R. Xu, H. C. Zhang, W. Z. Cai, M. Ni, M. L. Liu, Z. P. Shao, *Energy Environ. Sci.* **2017**, *10*, 2056.
10. T. L. Zhu, H. E. Troiani, L. V. Mogni, M. F. Han, S. A. Barnett, *Joule* **2018**, *2*, 478.
11. D. Dang, B. T. Zhao, D. C. Chen, B. M. deGlee, C. Qu, S. G. Dai, X. Y. Zeng, J. Liu, Y. F. Lu, S. J. Liao, M. L. Liu, *Energy Stor. Mater.* **2018**, *12*, 79.
12. Z. X. Song, B. Q. Wang, N. C. Cheng, L. J. Yang, D. Banham, R. Y. Li, S. Y. Ye, X. L. Sun, *J. Mater. Chem. A* **2017**, *5*, 9760.
13. Y. Feng, H. Liu, J. Yang, *Sci. Adv.* **2017**, *3*, e1700580.
14. Y. F. Song, W. Wang, L. Ge, X. M. Xu, Z. B. Zhang, P. Sergio, B. Juliao, W. Zhou, Z. P. Shao, *Adv. Sci.* **2017**, *4*, 1700337.
15. X. H. Chen, Y. Wang, L. Cai, Y. H. Zhou, *J. Power Sources* **2015**, *294*, 430.
16. Y. Zhang, L. Liu, B. Van der Bruggen, F. Yang, *J. Mater. Chem. A* **2017**, *5*, 12673.
17. Q. C. Liu, Z. W. Chang, Z. J. Li, X. B. Zhang, *Small Methods* **2018**, *2*, 1700231.
18. Z. Y. Guo, C. Li, J. Y. Liu, Y. G. Wang, Y. Y. Xia, *Angew. Chem. Int. Ed.* **2017**, *56*, 7505.
19. Q. Lu, J. Yu, X. Zou, K. Liao, P. Tan, W. Zhou, M. Ni, Z. Shao, *Adv. Funct. Mater.* **2019**, *29*, 1904481.
20. Y. G. Li, J. Lu, *ACS Energy Lett.* **2017**, *2*, 1370.
21. R. Jacobs, T. Mayeshiba, J. Booske, D. Morgan, *Adv. Energy Mater.* **2018**, *8*, 1702708.
22. J. Yu, G. Chen, J. Sunarso, Y. Zhu, R. Ran, Z. Zhu, W. Zhou, Z. Shao, *Adv. Sci.* **2016**, *3*, 1600060.
23. T. P. Zhou, W. F. Xu, N. Zhang, Z. Y. Du, C. G. Zhong, W. S. Yan, H. X. Ju, W. S. Chu, H. Jiang, C. Z. Wu, Y. Xie, *Adv. Mater.* **2019**, *31*, 1807468.
24. Y. C. Lu, Z. C. Xu, H. A. Gasteiger, S. Chen, K. Hamad-Schifferli, Y. Shao-Horn, *J. Am. Chem. Soc.* **2010**, *132*, 12170.
25. J. Yu, J. Sunarso, W. Zhuang, G. Yang, Y. Zhong, W. Zhou, Z. Zhu, Z. Shao, *Adv. Sustainable Syst.* **2017**, *1*, 1700045.
26. G. R. Zhang, S. Wollner, *Appl. Catal. B-Environ.* **2018**, *222*, 26.
27. S. Sui, X. Y. Wang, X. T. Zhou, Y. H. Su, S. Riffatc, C. J. Liu, *J. Mater. Chem. A* **2017**, *5*, 1808.
28. X. Y. Yang, J. J. Xu, Z. W. Chang, D. Bao, Y. B. Yin, T. Liu, J. M. Yan, D. P. Liu, Y. Zhang, X. B. Zhang, *Adv. Energy Mater.* **2018**, *8*, 1702242.
29. L. Yang, X. F. Zeng, W. C. Wang, D. P. Cao, *Adv. Funct. Mater.* **2018**, *28*, 1704537.
30. X. X. Wang, D. A. Cullen, Y. T. Pan, S. Hwang, M. Y. Wang, Z. X. Feng, J. Y. Wang, M. H. Engelhard, H. G. Zhang, Y. H. He, Y. Y. Shao, D. Su, K. L. More, J. S. Spendelow, G. Wu, *Adv. Mater.* **2018**, *30*, 1706758.
31. B. Liu, Y. L. Sun, L. Liu, S. Xu, X. B. Yan, *Adv. Funct. Mater.* **2018**, *28*, 1704973.
32. I. S. Amiinu, X. B. Liu, Z. H. Pu, W. Q. Li, Q. D. Li, J. Zhang, H. L. Tang, H. N. Zhang, S. C. Mu, *Adv. Funct. Mater.* **2018**, *28*, 1704638.

33. M. Li, M. Zhao, F. Li, W. Zhou, V. K. Peterson, X. Xu, Z. Shao, I. Gentle, Z. Zhu, *Nat. Commun.* **2017**, *8*, 13990.
34. P. Z. Li, B. Wei, Z. Lu, Y. Y. Wu, Y. H. Zhang, X. Q. Huang, *Appl. Surf. Sci.* **2019**, *464*, 494.
35. F. F. Lu, T. Xia, Q. Li, J. P. Wang, L. H. Huo, H. Zhao, *Appl. Catal. B-Environ.* **2019**, *249*, 19.
36. Z. X. Hao, R. Zeng, L. X. Yuan, Q. M. Bing, J. Y. Liu, J. W. Xiang, Y. H. Huang, *Nano Energy* **2017**, *40*, 360.
37. T. Liu, K. Yu, L. Gao, H. Chen, N. Wang, L. H. Hao, T. X. Li, H. C. He, Z. H. Guo, *J. Mater. Chem. A* **2017**, *5*, 17848.
38. J. Yu, J. Sunarso, Y. Zhu, X. Xu, R. Ran, W. Zhou, Z. Shao, *Chem. Eur. J.* **2016**, *22*, 2719.
39. L. Zhu, R. Ran, M. Tade, W. Wang, Z. Shao, *Asia-Pac. J. Chem. Eng.* **2016**, *11*, 338.
40. W. Wang, M. Xu, X. Xu, W. Zhou, Z. Shao, *Angew. Chem. Int. Ed.* **2019**, *58*, 2.
41. H. Zhang, D. Guan, X. Gao, J. Yu, G. Chen, W. Zhou, Z. Shao, *J. Mater. Chem. A* **2019**, *7*, 19228.
42. Y. Zhu, W. Zhou, J. Yu, Y. Chen, M. Liu, Z. Shao, *Chem. Mater.* **2016**, *28*, 1691.
43. Y. Zhu, W. Zhou, Y. Chen, J. Yu, X. Xu, C. Su, M. O. Tadé, Z. Shao, *Chem. Mater.* **2015**, *27*, 3048.
44. X. Xu, C. Su, W. Zhou, Y. Zhu, Y. Chen, Z. Shao, *Adv. Sci.* **2016**, *3*, 1500187.
45. J. Suntivich, K. J. May, H. A. Gasteiger, J. B. Goodenough, Y. Shao-Horn, *Science* **2011**, *334*, 1383.
46. J. Suntivich, H. A. Gasteiger, N. Yabuuchi, H. Nakanishi, J. B. Goodenough, Y. Shao-Horn, *Nat. Chem.* **2011**, *3*, 546.
47. D. Meadowcroft, *Nature* **1970**, *226*, 847.
48. J. O. M. Bockris, T. Otagawa, *J. Electrochem. Soc.* **1984**, *131*, 290.
49. S. Tiwari, J. Koenig, G. Poillerat, P. Chartier, R. Singh, *J. Appl. Electrochem.* **1998**, *28*, 114.
50. W. Zhou, M. Zhao, F. Liang, S. C. Smith, Z. Zhu, *Mater. Horiz.* **2015**, *2*, 495.
51. B. T. Zhao, L. Zhang, D. X. Zhen, S. Yoo, Y. Ding, D. C. Chen, Y. Chen, Q. B. Zhang, B. Doyle, X. H. Xiong, M. L. Liu, *Nat. Commun.* **2017**, *8*, 14586.
52. Y. L. Zhu, W. Zhou, Z. G. Chen, Y. B. Chen, C. Su, M. O. Tade, Z. P. Shao, *Angew. Chem. Int. Ed.* **2015**, *54*, 3897.
53. X. Xu, W. Wang, W. Zhou, Z. Shao, *Small Methods* **2018**, *2*, 1800071.
54. Z. C. Wang, W. J. Xu, X. K. Chen, Y. H. Peng, Y. Y. Song, C. X. Lv, H. L. Liu, J. W. Sun, D. Yuan, X. Y. Li, X. X. Guo, D. J. Yang, L. X. Zhang, *Adv. Funct. Mater.* **2019**, *29*, 1902875.
55. H. Jiang, J. X. Gu, X. S. Zheng, M. Liu, X. Q. Qiu, L. B. Wang, W. Z. Li, Z. F. Chen, X. B. Ji, J. Li, *Energy Environ. Sci.* **2019**, *12*, 322.
56. Y.-F. Sun, Y.-Q. Zhang, Y.-L. Yang, J. Chen, B. Hua, Y.-X. Shi, C.-A. Wang, J.-L. Luo, *Appl. Catal. B-Environ.* **2017**, *219*, 640.
57. Y. Yang, W. Zhou, R. Liu, M. Li, T. E. Rufford, Z. Zhu, *ChemElectroChem* **2015**, *2*, 200.
58. Y. Xu, A. Tsou, Y. Fu, J. Wang, J.-H. Tian, R. Yang, *Electrochim. Acta* **2015**, *174*, 551.
59. P. Sennu, V. Aravindan, K. S. Nahm, Y.-S. Lee, *J. Mater. Chem. A* **2017**, *5*, 18029.
60. X. Han, Y. Hu, J. Yang, F. Cheng, J. Chen, *Chem. Commun.* **2014**, *50*, 1497.
61. Y. Bu, O. Gwon, G. Nam, H. Jang, S. Kim, Q. Zhong, J. Cho, G. Kim, *ACS Nano* **2017**, *11*, 11594.
62. A. Ashok, A. Kumar, R. R. Bhosale, F. Almomani, S. S. Malik, S. Suslov, F. Tarlochan, *J. Electroanaly. Chem.* **2018**, *809*, 22.
63. Y. Zhu, W. Zhou, Y. Zhong, Y. Bu, X. Chen, Q. Zhong, M. Liu, Z. Shao, *Adv. Energy Mater.* **2017**, *7*, 1602122.
64. Y. Zhao, L. Xu, L. Mai, C. Han, Q. An, X. Xu, X. Liu, Q. Zhang, *P. Natl. Acad. Sci. USA* **2012**, *109*, 19569.
65. X. Li, H. Dai, J. Deng, Y. Liu, Z. Zhao, Y. Wang, H. Yang, C. T. Au, *Appl. Catal. A-Gen.* **2013**, *458*, 11.
66. S. Jiang, F. Liang, W. Zhou, Z. Shao, *J. Mater. Chem.* **2012**, *22*, 16214.
67. J. He, W. Zhou, J. Sunarso, X. Xu, Y. Zhong, Z. Shao, X. Chen, H. Zhu, *Electrochim. Acta* **2018**, *260*, 372.
68. S. Song, J. Zhou, S. Zhang, L. Zhang, J. Li, Y. Wang, L. Han, Y. Long, Z. Hu, J.-Q. Wang, *Nano Res.* **2018**, *11*, 4796.

69. S. Zhuang, C. Huang, K. Huang, X. Hu, F. Tu, H. Huang, *Electrochem. Commun*. **2011**, *13*, 321.
70. C. Jin, X. Cao, F. Lu, Z. Yang, R. Yang, *Int. J. Hydrogen Energy* **2013**, *38*, 10389.
71. P. V. Gosavi, R. B. Biniwale, *Mater. Chem. Phys.* **2010**, *119*, 324.
72. J. Kim, X. Chen, P.-C. Shih, H. Yang, *ACS Sustainable Chem. Eng.* **2017**, *5*, 10910.
73. T. V. Pham, H. P. Guo, W. B. Luo, S. L. Chou, J. Z. Wang, H. K. Liu, *J. Mater. Chem. A* **2017**, *5*, 5283.
74. B. Hua, M. Li, Y. Q. Zhang, Y. F. Sun, J. L. Luo, *Adv. Energy Mater.* **2017**, *7*, 1700666.
75. D. Zhen, B. Zhao, H. C. Shin, Y. Bu, Y. Ding, G. He, M. Liu, *Adv. Mater. Interfaces* **2017**, *4*, 1700146.
76. Z. Shao, W. Zhou, Z. Zhu, *Prog. Mater. Sci.* **2012**, *57*, 804.
77. Z. Shen, X. Wang, B. Luo, L. Li, *J. Mater. Chem. A* **2015**, *3*, 18146.
78. Y. Zhu, W. Zhou, J. Sunarso, Y. Zhong, Z. Shao, *Adv. Funct. Mater.* **2016**, *26*, 5862.
79. Z. Zhang, Y. Chen, M. O. Tade, Y. Hao, S. Liu, Z. Shao, *J. Mater. Chem. A* **2014**, *2*, 9666.
80. S. S. Pramana, A. Cavallaro, C. Li, A. D. Handoko, K. W. Chan, R. J. Walker, A. Regoutz, J. S. Herrin, B. S. Yeo, D. J. Payne, *J. Mater. Chem. A* **2018**, *6*, 5335.
81. Y. Chen, H. Li, J. Wang, Y. Du, S. Xi, Y. Sun, M. Sherburne, J. W. Ager, A. C. Fisher, Z. J. Xu, *Nat. Commun.* **2019**, *10*, 572.
82. H. Sun, G. Chen, J. Sunarso, J. Dai, W. Zhou, Z. Shao, *ACS Appl. Mater. Interfaces* **2018**, *10*, 16939.
83. H. Liu, X. Ding, L. Wang, D. Ding, S. Zhang, G. Yuan, *Electrochim. Acta* **2018**, *259*, 1004.
84. N. Tien-Thao, M. H. Zahedi-Niaki, H. Alamdari, S. Kaliaguine, *J. Catal.* **2007**, *245*, 348.
85. R. Li, K. Liao, W. Zhou, X. Li, D. Meng, R. Cai, Z. Shao, *J. Membrane Sci.* **2019**, *582*, 194.
86. R. Yu, Q.-X. Du, B.-K. Zou, Z.-Y. Wen, C.-H. Chen, *J. Power Sources* **2016**, *306*, 623.
87. E. Mendoza-Mendoza, K. P. Padmasree, S. M. Montemayor, A. F. Fuentes, *J. Mater. Sci.* **2012**, *47*, 6076.
88. X. H. Huang, H. Y. Pan, K. Chen, Z. L. Yin, J. Hong, *Crystengcomm* **2018**, *20*, 7020.
89. Y. Z. Wang, S. H. Xie, J. G. Deng, S. X. Deng, H. Wang, H. Yan, H. X. Dai, *ACS Appl. Mater. Interfaces* **2014**, *6*, 17394.
90. X. Xu, Y. Pan, W. Zhou, Y. Chen, Z. Zhang, Z. Shao, *Electrochim. Acta* **2016**, *219*, 553.
91. J. F. Shin, W. Xu, M. Zanella, K. Dawson, S. N. Savvin, J. B. Claridge, M. J. Rosseinsky, *Nat. Energy* **2017**, *2*, 16214.
92. H. Sun, J. He, Z. Hu, C.-T. Chen, W. Zhou, Z. Shao, *Electrochim. Acta* **2019**, *299*, 926.
93. G. Yang, W. Zhou, M. Liu, Z. Shao, *ACS Appl. Mater. Interfaces* **2016**, *8*, 35308.
94. E. M. Zahrani, M. Fathi, *Ceram. Int.* **2009**, *35*, 2311.
95. R. Zhang, H. Alamdari, S. Kaliaguine, *Appl. Catal. A-Gen.* **2008**, *340*, 140.
96. S. Royer, F. Berube, S. Kaliaguine, *Appl. Catal. A-Gen.* **2005**, *282*, 273.
97. L. H. Li, J. X. Deng, J. Chen, X. R. Xing, *Chem. Sci.* **2016**, *7*, 855.
98. Y.-L. Song, Z.-C. Wang, Y.-D. Yan, M.-L. Zhang, G.-L. Wang, T.-Q. Yin, Y. Xue, F. Gao, M. Qiu, *J. Energy Chem.* **2020**, *43*, 173.
99. X. Liu, L. S. Wang, Y. T. Ma, H. F. Zheng, L. Lin, Q. F. Zhang, Y. Z. Chen, Y. L. Qiu, D. L. Peng, *ACS Appl. Mater. Interfaces* **2017**, *9*, 7601.
100. N. Fechler, T.-P. Fellinger, M. Antonietti, *Adv. Mater.* **2013**, *25*, 75.
101. X. Liu, M. Antonietti, *Adv. Mater.* **2013**, *25*, 6284.
102. Y. Mao, S. Banerjee, S. S. Wong, *J. Am. Chem. Soc.* **2003**, *125*, 15718.
103. M. Kačenka, O. Kaman, Z. Jirák, M. Maryško, P. Veverka, M. Veverka, S. Vratislav, *J. Solid State Chem.* **2015**, *221*, 364.
104. F. Li, X. Yu, L. Chen, H. Pan, X. Xin, *J. Am. Ceram. Soc.* **2002**, *85*, 2177.
105. X. Deng, B. T. Zhao, L. Zhu, Z. P. Shao, *Carbon* **2015**, *93*, 48.
106. H. Zhou, Y. Mao, S. S. Wong, *Chem. Mater.* **2007**, *19*, 5238.
107. J. Kim, X. Yin, K.-C. Tsao, S. Fang, H. Yang, *J. Am. Chem. Soc.* **2014**, *136*, 14646.
108. N. Pinna, M. Niederberger, *Angew. Chem. Int. Ed.* **2008**, *47*, 5292.
109. J. Park, J. Joo, S. G. Kwon, Y. Jang, T. Hyeon, *Angew. Chem. Int. Ed.* **2007**, *46*, 4630.
110. L. Zhang, I. Djerdj, M. Cao, M. Antonietti, M. Niederberger, *Adv. Mater.* **2007**, *19*, 2083.
111. M. Niederberger, N. Pinna, J. Polleux, M. Antonietti, *Angew. Chem. Int. Ed.* **2004**, *43*, 2270.

112. M. Niederberger, G. Garnweitner, N. Pinna, M. Antonietti, *J. Am. Chem. Soc.* **2004**, *126*, 9120.
113. N. Y. Chan, M. Zhao, J. Huang, K. Au, M. H. Wong, H. M. Yao, W. Lu, Y. Chen, C. W. Ong, H. L. W. Chan, *Adv. Mater.* **2014**, *26*, 5962.
114. J. X. Wang, Y. K. Tao, J. Shao, W. G. Wang, *J. Power Sources* **2009**, *186*, 344.
115. H. Bessbousse, I. Nandhakumar, M. Decker, M. Barsbay, O. Cuscito, D. Lairez, M.-C. Clochard, T. L. Wade, *Anal. Methods* **2011**, *3*, 1351.
116. S. She, J. Yu, W. Tang, Y. Zhu, Y. Chen, J. Sunarso, W. Zhou, Z. Shao, *ACS Appl. Mater. Interfaces* **2018**, *10*, 11715.
117. W. Zhou, J. Sunarso, *J.Phys. Chem. Lett.* **2013**, *4*, 2982.
118. X. Xu, Y. Chen, W. Zhou, Z. Zhu, C. Su, M. Liu, Z. Shao, *Adv. Mater.* **2016**, *28*, 6442.
119. S. T. Aruna, A. S. Mukasyan, *Curr. Opin. Solid State Mater. Sci.* **2008**, *12*, 44.
120. D. P. Tarragó, C. de Fraga Malfatti, V. C. de Sousa, *Powder Technol.* **2015**, *269*, 481.
121. A. Greiner, J. H. Wendorff, *Angew. Chem. Int. Ed.* **2007**, *46*, 5670.
122. J. J. Xue, T. Wu, Y. Q. Dai, Y. N. Xia, *Chem. Rev.* **2019**, *119*, 5298.
123. J. Zhang, Y. Zhao, X. Zhao, Z. Liu, W. Chen, *Sci. Rep.* **2014**, *4*, 6005.
124. A. Vignesh, M. Prabu, S. Shanmugam, *ACS Appl. Mater. Interfaces* **2016**, *8*, 6019.
125. Z. Wang, M. Li, C. Liang, L. Fan, J. Han, Y. Xiong, *RSC Adv.* **2016**, *6*, 69251.
126. T. D. Thanh, N. D. Chuong, J. Balamurugan, H. Van Hien, N. H. Kim, J. H. Lee, *Small* **2017**, *13*, 1701884.
127. H. W. Park, D. U. Lee, P. Zamani, M. H. Seo, L. F. Nazar, Z. Chen, *Nano Energy* **2014**, *10*, 192.
128. M. Prabu, P. Ramakrishnan, P. Ganesan, A. Manthiram, S. Shanmugam, *Nano Energy* **2015**, *15*, 92.
129. K. Stephan, M. Hackenberger, D. Kiessling, G. Wendt, *Catal. Today* **1999**, *54*, 23.
130. N. Yi, Y. Cao, Y. Su, W.-L. Dai, H.-Y. He, K.-N. Fan, *J. Catal.* **2005**, *230*, 249.
131. M. Alifanti, M. Florea, S. Somacescu, V. Parvulescu, *Appl. Catal. B-Environ.* **2005**, *60*, 33.
132. G. Kim, S. Lee, J. Shin, G. Corre, J. Irvine, J. Vohs, R. J. Gorte, *Electrochem. Solid State Lett.* **2009**, *12*, B48.
133. M. Alifanti, M. Florea, V. I. Pârvulescu, *Appl. Catal. B-Environ.* **2007**, *70*, 400.
134. R. R. Ding, J. N. Hu, R. S. Hu, Y. Liu, L. J. Wang, *Adv. Mater. Research* **2012**, *512*, 1601.
135. S. Keav, S. K. Matam, D. Ferri, A. Weidenkaff, *Catalysts* **2014**, *4*, 226.
136. F. Lu, J. Sui, J. Su, C. Jin, M. Shen, R. Yang, *J. Power Sources* **2014**, *271*, 55.
137. Y. Yang, W. Yin, S. Wu, X. Yang, W. Xia, Y. Shen, Y. Huang, A. Cao, Q. Yuan, *ACS Nano* **2015**, *10*, 1240.
138. M. Baythoun, F. Sale, *J. Mater. Sci.* **1982**, *17*, 2757.
139. S. Zhou, X. Miao, X. Zhao, C. Ma, Y. Qiu, Z. Hu, J. Zhao, L. Shi, J. Zeng, *Nat. Commun.* **2016**, *7*, 11510.
140. C. Chen, J. Cheng, S. Yu, L. Che, Z. Meng, *J. Cryst. Growth* **2006**, *291*, 135.
141. Y. Mao, S. Banerjee, S. S. Wong, *Chem. Commun.* **2003**, *3*, 408.
142. M. Pena, J. Fierro, *Chem. Rev.* **2001**, *101*, 1981.
143. T. Valdés-Solís, G. Marbán, A. Fuertes, *Chem. Mater.* **2005**, *17*, 1919.
144. S. Royer, D. Duprez, F. Can, X. Courtois, C. Batiot-Dupeyrat, S. Laassiri, H. Alamdari, *Chem. Rev.* **2014**, *114*, 10292.
145. N. Pal, M. Paul, A. Bhaumik, *Appl. Catal. A-Gen.* **2011**, *393*, 153.
146. J. J. Xu, D. Xu, Z. L. Wang, H. G. Wang, L. L. Zhang, X. B. Zhang, *Angew. Chem. Int. Ed.* **2013**, *52*, 3887.
147. Y.-C. Lee, P.-Y. Peng, W.-S. Chang, C.-M. Huang, *J. Taiwan Inst. Chem. Eng.* **2014**, *45*, 2334.
148. F. Lu, Y. Wang, C. Jin, F. Li, R. Yang, F. Chen, *J. Power Sources* **2015**, *293*, 726.
149. F. Schüth, *Angew. Chem. Int. Ed.* **2003**, *42*, 3604.
150. Y. Wang, J. Ren, Y. Wang, F. Zhang, X. Liu, Y. Guo, G. Lu, *J. Phys. Chem. C* **2008**, *112*, 15293.
151. M. M. Nair, F. Kleitz, S. Kaliaguine, *ChemCatChem* **2012**, *4*, 387.
152. Z. Zhao, H. Dai, J. Deng, Y. Du, Y. Liu, L. Zhang, *Micropor. Mesopor. Mater.* **2012**, *163*, 131.
153. R. De Lima, M. Batista, M. Wallau, E. Sanches, Y. P. Mascarenhas, E. Urquieta-González, *Appl. Catal. B-Environ.* **2009**, *90*, 441.

154. W. Zhou, R. Ran, Z. Shao, W. Jin, N. Xu, *Bull. Mater. Sci.* **2010**, *33*, 371.
155. J. Dai, Y. Zhu, Y. Zhong, J. Miao, B. Lin, W. Zhou, Z. Shao, *Adv. Mater. Interfaces* **2019**, *6*, 1801317.
156. M. Schwickardi, T. Johann, W. Schmidt, F. Schüth, *Chem. Mater.* **2002**, *14*, 3913.
157. X. Fan, Y. Wang, X. Chen, L. Gao, W. Luo, Y. Yuan, Z. Li, T. Yu, J. Zhu, Z. Zou, *Chem. Mater.* **2010**, *22*, 1276.
158. F. Zou, Z. Jiang, X. Qin, Y. Zhao, L. Jiang, J. Zhi, T. Xiao, P. P. Edwards, *Chem. Commun.* **2012**, *48*, 8514.
159. H. Lu, P. Zhang, Z.-A. Qiao, J. Zhang, H. Zhu, J. Chen, Y. Chen, S. Dai, *Chem. Commun.* **2015**, *51*, 5910.
160. C. K. Chan, H. Peng, G. Liu, K. McIlwrath, X. F. Zhang, R. A. Huggins, Y. Cui, *Nat. Nanotechnol.* **2008**, *3*, 31.
161. Y. Li, P. Hasin, Y. Wu, *Adv. Mater.* **2010**, *22*, 1926.
162. K. Song, E. Cho, Y.-M. Kang, *ACS Catal.* **2015**, *5*, 5116.
163. P. Tan, M. Liu, Z. Shao, M. Ni, *Adv. Energy Mater.* **2017**, *7*, 1602674.
164. J. Park, J. Jeong, S. Lee, C. Jo, J. Lee, *ChemSusChem* **2015**, *8*, 3146.
165. O.-H. Kim, Y.-H. Cho, S. H. Kang, H.-Y. Park, M. Kim, J. W. Lim, D. Y. Chung, M. J. Lee, H. Choe, Y.-E. Sung, *Nat. Commun.* **2013**, *4*, 2473.
166. Y. Zhu, W. Zhou, Z. Shao, *Small* **2017**, *13*, 1603793.
167. H. Liu, J. Yu, J. Sunarso, C. Zhou, B. Liu, Y. Shen, W. Zhou, Z. Shao, *Electrochim. Acta* **2018**, *282*, 324.
168. H. Zhu, P. Zhang, S. Dai, *ACS Catal.* **2015**, *5*, 6370.
169. F. Bertocci, A. Fort, V. Vignoli, M. Mugnaini, R. Berni, *Sensors* **2017**, *17*, 1352.
170. J. He, J. Sunarso, Y. Zhu, Y. Zhong, J. Miao, W. Zhou, Z. Shao, *Sens. Actuators B Chem.* **2017**, *244*, 482.
171. M. Xu, W. Wang, Y. Liu, Y. Zhong, X. Xu, Y. Sun, J. Wang, W. Zhou, Z. Shao, *Solar RRL* **2019**, *3*, 1970075.
172. W. Wang, R. Tran, J. Qu, Y. Liu, C. Chen, M. Xu, Y. Chen, S. P. Ong, L. Wang, W. Zhou, *ACS Appl. Mater. Interfaces* **2019**, *11*, 35641.
173. J. Wang, Z. Liu, Y. Zheng, L. Cui, W. Yang, J. Liu, *J. Mater. Chem. A* **2017**, *5*, 22913.
174. L. D. Fan, B. Zhu, P. C. Su, C. X. He, *Nano Energy* **2018**, *45*, 148.
175. S. B. Adler, J. A. Lane, B. C. H. Steele, *J. Electrochem. Soc.* **1996**, *143*, 3554.
176. M. Mamak, N. Coombs, G. Ozin, *J. Am. Chem. Soc.* **2000**, *122*, 8932.
177. Y. L. Zhang, S. W. Zha, M. L. Liu, *Adv. Mater.* **2005**, *17*, 487.
178. F. Zhao, Z. Wang, M. Liu, L. Zhang, C. Xia, F. Chen, *J. Power Sources* **2008**, *185*, 13.
179. C. Yang, A. Coffin, F. Chen, *Int. J. Hydrogen Energy* **2010**, *35*, 3221.
180. W. Zhou, F. L. Liang, Z. P. Shao, Z. H. Zhu, *Sci. Rep.* **2012**, *2*, 327.
181. J. G. Lee, J. H. Park, Y. G. Shul, *Nat. Commun.* **2014**, *5*, 4045.
182. Y. Chen, Y. Lin, Y. Zhang, S. Wang, D. Su, Z. Yang, M. Han, F. Chen, *Nano Energy* **2014**, *8*, 25.
183. Y. Chen, Y. Bu, Y. Zhang, R. Yan, D. Ding, B. Zhao, S. Yoo, D. Dang, R. Hu, C. Yang, *Adv. Energy Mater.* **2017**, *7*, 1601890.
184. F. Li, Z. Tao, H. Dai, X. Xi, H. Ding, *Int. J. Hydrogen Energy* **2018**, *43*, 19757.
185. S. U. Rehman, R.-H. Song, T.-H. Lim, S.-J. Park, J.-E. Hong, J.-W. Lee, S.-B. Lee, *J. Mater. Chem. A* **2018**, *6*, 6987.
186. Y. Song, W. Wang, L. Ge, X. Xu, Z. Zhang, P. S. B. Julião, W. Zhou, Z. Shao, *Adv. Sci.* **2017**, *4*, 1700337.
187. N. Yu, L. Kuai, Q. Wang, B. Geng, *Nanoscale* **2012**, *4*, 5386.
188. P. G. Bruce, S. A. Freunberger, L. J. Hardwick, J.-M. Tarascon, *Nat. Mater.* **2012**, *11*, 19.
189. H.-F. Wang, C. Tang, Q. Zhang, *Adv. Funct. Mater.* **2018**, *28*, 1803329.
190. J. Pan, X. L. Tian, S. Zaman, Z. H. Dong, H. F. Liu, H. S. Park, B. Y. Xia, *Batteries & Supercaps* **2019**, *2*, 336.
191. J. G. Kim, Y. Kim, Y. Noh, S. Lee, Y. Kim, W. B. Kim, *ACS Appl. Mater. Interfaces* **2018**, *10*, 5429.
192. X. Chen, S. Chen, B. Nan, F. Jia, Z. Lu, H. Deng, *Ionics* **2017**, *23*, 2241.

193. J.-J. Xu, Z.-L. Wang, D. Xu, F.-Z. Meng, X.-B. Zhang, *Energy Environ. Sci.* **2014**, *7*, 2213.
194. Y.-W. Ju, S. Yoo, L. Guo, C. Kim, A. Inoishi, H. Jeong, J. Shin, T. Ishihara, S.-D. Yim, G. Kim, *J. Electrochem. Soc.* **2015**, *162*, A2651.
195. M. Y. Oh, J. J. Lee, A. Zahoor, K. S. Nahm, *RSC Adv.* **2016**, *6*, 32212.
196. P. Li, J. Zhang, Q. Yu, J. Qiao, Z. Wang, D. Rooney, W. Sun, K. Sun, *Electrochim. Acta* **2015**, *165*, 78.
197. G. Liu, H. Chen, L. Xia, S. Wang, L.-X. Ding, D. Li, K. Xiao, S. Dai, H. Wang, *ACS Appl. Mater. Interfaces* **2015**, *7*, 22478.
198. Y. Gong, X. Zhang, Z. Li, Z. Wang, C. Sun, L. Chen, *ChemNanoMat* **2017**, *3*, 485.
199. X. Zhang, Y. Gong, S. Li, C. Sun, *ACS Catal.* **2017**, *7*, 7737.
200. Y. Wang, X. Cui, Y. Li, L. Chen, Z. Shu, H. Chen, J. Shi, *Dalton Trans.* **2013**, *42*, 9448.
201. L. Kuai, E. Kan, W. Cao, M. Huttula, S. Ollikkala, T. Ahopelto, A.-P. Honkanen, S. Huotari, W. Wang, B. Geng, *Nano Energy* **2018**, *43*, 81.
202. J. Hu, Q. N. Liu, Z. W. Shi, L. Zhang, H. Huang, *RSC Adv.* **2016**, *6*, 86386.
203. Y. Hu, X. Han, Q. Zhao, J. Du, F. Cheng, J. Chen, *J. Mater. Chem. A* **2015**, *3*, 3320.